catalysts

MDPI

*Review*

# Advancements in Solar Desalination of Seawater by Various $Ti_3C_2$ MXene Based Morphologies for Freshwater Generation: A Review

**Adem Sreedhar and Jin-Seo Noh ***

Department of Physics, Gachon University, 1342 Seongnamdaero, Sujeong-gu, Seongnam-si 461-701, Gyeonggi-do, Korea; ademgu@gachon.ac.kr
* Correspondence: jinseonoh@gachon.ac.kr

**Abstract:** For a few years, we have been witnessing ubiquitous fresh and drinking water scarcity in various countries. To mitigate these problematic situations, many countries relied on non-conventional freshwater generation technologies through solar desalination of seawater. In this manner, we excel the ability of new class 2D $Ti_3C_2$ MXenes as a photothermal material (solar absorber) for freshwater generation via the solar desalination technique. In this review, the air–water interfacial interaction is highlighted for improving the evaporation efficiency. To provide the dependence of the desalination efficiency on the microstructure of the solar absorbers, we summarized various forms of 2D $Ti_3C_2$ MXenes (aerosol, films, foam, hydrogel, membrane, monolith and porous structure) and their characteristics. These microstructures prevailed ultrahigh photoconversion efficiency. In this aspect, we further explained key features such as light absorption, reflection, multiple internal reflection, hydrophilicity, lower thermal conduction, light-to-heat generation, and salt rejection for achieving efficient desalination output throughout the visible and broadband region. Specifically, we targeted to explore the self-floating and salt rejection nature of various state-of-the-art 2D $Ti_3C_2$ MXene structures. Further, we highlighted the long-term stability. Among the above morphologies, $Ti_3C_2$ MXene in the form of a membrane is believed to be a promising morphology which effectively desalinates seawater into freshwater. Finally, we highlighted the challenges and future perspectives, which can pave a potential path for advancing the sustainable solar desalination of seawater into freshwater.

**Keywords:** 2D $Ti_3C_2$ MXene; membrane; broadband; solar desalination; freshwater



**Citation:** Sreedhar, A.; Noh, J.-S. Advancements in Solar Desalination of Seawater by Various $Ti_3C_2$ MXene Based Morphologies for Freshwater Generation: A Review. *Catalysts* **2021**, *11*, 1435. https://doi.org/10.3390/catal11121435

Academic Editors: Carolina Belver and Jorge Bedia

Received: 29 October 2021
Accepted: 23 November 2021
Published: 25 November 2021



## 1. Introduction

Water is the most essential resource for life on the earth. Due to the enormous growth of population and industrialization, our ecological system is significantly facing freshwater scarcity and contamination. At the same time, the availability of freshwater on the earth is 3% only [1]. Additionally, yearly, one-third of the population is not in a position to access fresh drinking water [2]. Thus, the production of freshwater from abundantly available seawater is necessary under eco-friendly techniques because conventional wastewater purification methods consume high energy [3]. Reverse osmosis (RO) and pervaporation (PV) proved their importance for the desalination process [4–6]. However, RO requires high pressure to conquer the osmotic pressure of seawater [7]. Additionally, the processing of RO is cost-effective, and maintenance is associated with scaling, fouling, and degradation. This energy-intensive technique has a huge impact on the economy (high energy demand) and environment ($CO_2$ emissions). For a decade, the desalination process has been skyrocketing in various countries. There is another interesting technology, such as capacitive deionization (CDI), which yields desalination efficiency under low energy consumption under an ecofriendly process [8]. Specifically, water scarcity becomes ever more threatening. For this, many countries permanently rely on these techniques. Thus,

it is the right time to develop an advanced, eco-friendly, 100% carbon neutral, harmless, and low-cost desalination technique. In such a way, the solar desalination process raised its importance through the harvesting of the abundantly available solar energy into steam (freshwater) under the strategic conversion of light into heat [9]. For example, solar desalination is a process for obtaining pure water from abundantly available seawater through the pressure-free water purification process. It is to be noted that renewable solar energy is highly beneficial, which is an alternative to the utilization of carbon emissive fossil fuels (oil, coal, and gas). Thus, we can nullify the emission of carbon byproducts by utilizing renewable solar energy. Specifically, challenges associated with the developed solar absorber during the water evaporation process are (i) extended light absorption throughout the solar spectrum, (ii) the hydrophilic nature, (iii) low thermal conductivity, and (iv) high electrical conductivity. On the other hand, we should focus on crystallization of salt on the absorber. This process suppresses the water transport channel, localization of heat, and freshwater production under reduced energy conversion. We should further focus on solar desalination not only on a sunny day, but also under complex conditions, such as cloudy, rainy, or night conditions.

Transition metal carbides are effectively used as electrocatalysts for oxygen evolution reactions [10]. Due to the conceivable photocatalytic activity of $Ti_3C_2$ MXene [11], porous structured novel 2D MXenes raised its importance in the field of desalination of seawater under strategic utilization of abundant solar electromagnetic spectrum. It should be noted that 2D $Ti_3C_2$ MXene can absorb near-infrared light for the photofixation of $N_2$ [12]. Additionally, $Ti_3C_2$ MXene proved superior photothermal conversion efficiency of 100% (theoretical), which paved a potential path for the absorption and conversion of electromagnetic radiation into heat [13], which is one of the required features for advancing the water evaporation process. These features guarantee the solar desalination of 2D $Ti_3C_2$ MXene under controlled interfacial interaction with various semiconducting materials. Therefore, the developing of highly surface-active $Ti_3C_2$ MXene-based binary or ternary composites effectively converts incident light into heat under solar and IR/NIR regions, which is urgently required. In addition, strengthened surface termination groups (-OH, -O, and -F) during the formation of $Ti_3C_2$ MXene from its precursor ($Ti_3AlC_2$ MAX phase) provide impressive optical properties [14], which further boost the overall solar desalination process.

Indeed, the morphology of the developed $Ti_3C_2$ MXene is considered a promising feature during the desalination process for the efficient absorption of seawater. Significant research is going on for controlling the surface morphological features of $Ti_3C_2$ MXene to provide the right water transportation channels and efficient saltwater desalination. Thus, it is necessary to estimate the desalination efficiency of $Ti_3C_2$ MXene under various surface morphological features. Many morphologies, such as aerosol [15], films [16], foam [17], hydrogel [18], membrane [19], monolith [20] and porous structure [21] have been extracted from layer structured 2D $Ti_3C_2$ MXenes. Among the large community of the MXene family, $Ti_3C_2$ MXene is skyrocketing in various energy conversion applications, such as hydrogen production [22], dye degradation [23], drug degradation [24], $CO_2$ reduction [25,26], $N_2$ reduction [12,27], triboelectric nanogenerator [28], supercapacitor [29], solar cells [30,31], etc.

Based on the above constructive features, we have comprehensively summarized the innovative desalination capacity of various $Ti_3C_2$ MXene morphologies. This review mainly involved the reliability of the $Ti_3C_2$ MXenes morphology, which greatly enhances the desalination ability. There is scarce research on the development of optimized photothermal $Ti_3C_2$ MXene materials and the design of prototypes. In such a way, we provided the effectiveness of the $Ti_3C_2$ MXene morphology for sustainable solar desalination by converting light into heat and then water vapor. Until now, there were very few review articles and research articles published based on $Ti_3C_2$ MXenes for solar desalination [1,32]. Thus, 2D $Ti_3C_2$ MXene as an advanced material provides the innovative paths and technological solutions for freshwater generation. Understanding the oxidation ability of $Ti_3C_2$ MXene during the desalination process also provides a benchmark for realizing long-term stability.

## 2. Desalination

The production of freshwater (low salinity) from the abundantly available seawater (high salinity) is known as desalination. Majorly, the water available on earth is about 97% and it is saline in nature because 70% of earth is covered by the oceans, which means we only get 3% of freshwater for daily and industrial purposes [33]. Desalination is a non-conventional freshwater generation process, which is currently fulfilling 1% of the world's fresh drinking water. During the thermal (distillation) or mechanical (RO) desalination process, high energy and pressure conditions are necessary. Currently, multi-stage flash distillation (thermal energy) and RO using membranes (mechanical energy) are majorly used for desalination. Here, RO requires less energy compared to multi-stage flash distillation. During the RO desalination process, high pressure pumps the seawater through the membrane, which results in low-pressure freshwater and high-pressure brine. Due to the high energy consumption during the above desalination processes, the development of a facile desalination process by utilizing a renewable energy resource (solar energy) is desirable. Despite the reliability of the RO process, significant efforts have been focusing on pressure-free and low energy consumption desalination processes. In this category, the generation of freshwater vapor from seawater using a photothermal material under abundant solar light is skyrocketing. Figure 1 presents the cost-effective schematic representation of solar desalination of seawater into freshwater under solar light, using novel 2D layer structured $Ti_3C_2$ MXenes.

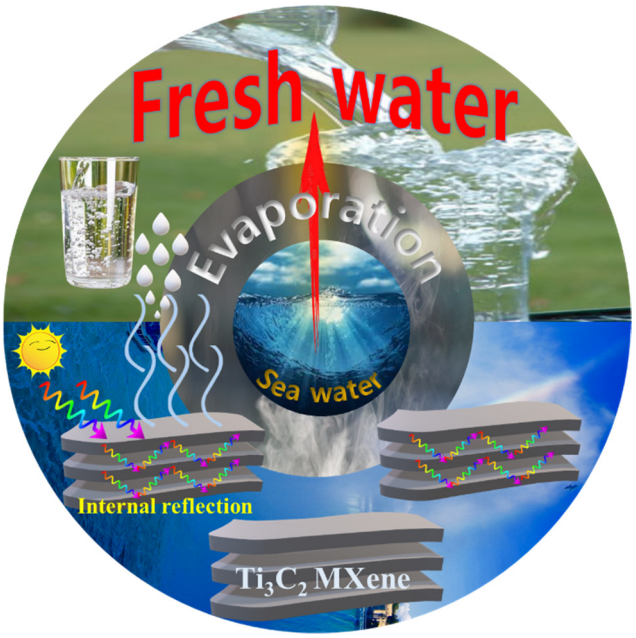


**Figure 1.** Schematic representation of seawater to freshwater generation by the 2D layer structured $Ti_3C_2$ MXenes.

## 3. Key Factors for Achieving Superior Solar Desalination

It is necessary to develop a stable photothermal material which address the desalination ability throughout the solar spectrum. For this, we should conquer few key points during the desalination process. These features make a potential path to realize the solar-driven water purification process. Therefore, we have provided the following fundamental features which profoundly demonstrate the effectiveness of the solar desalination of seawater into freshwater.

### *3.1. Control on Heat Loss*

To convert saline seawater into freshwater, the developed photothermal material should overcome three kinds of heat losses: (i) radiation, (ii) convection, and (iii) con-

duction. Specifically, heat localization is the underlying parameter for advancing the exceptional solar-to-vapor efficiency during the desalination process [34]. All these factors make standalone solar evaporators for productive freshwater generation. For instance, it is necessary to develop a low thermal conductive material to localize the heat at the interface of water–air during the desalination process. At suppressed heat loss toward the bulk water, the localized heat effect significantly improves the steam generation. Figure 2 presents the schematic representation and key factors, which greatly influence the solar desalination by the layer structured 2D $Ti_3C_2$ MXenes. Specifically, lowering the thermal conduction, radiation, and convection at improved internal reflection greatly improves the overall water evaporation rate.

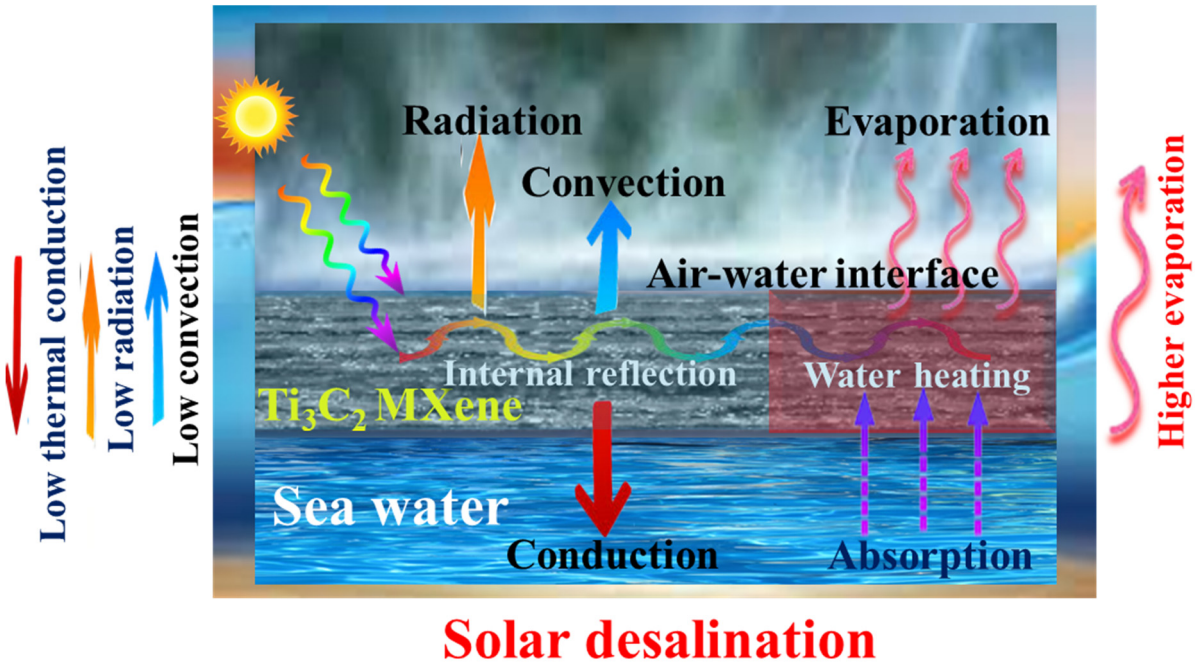


**Figure 2.** Prominent figures of merits of $Ti_3C_2$ MXenes during solar desalination process.

### *3.2. Reduced Light Reflection, Transmission, and Improved Broadband Light Absorption*

In addition to the above features, light absorption, transmission, and reflection also determine the solar conversion efficiency. Reduced light reflection and improved absorption make more light-to-heat generation capacity by the photothermal materials (solar absorber). For this, we require various morphological and microstructure designs, which eventually improved the light absorption capacity under reduced reflection [35]. On the other hand, we should suppress the transmittance toward the bulk water. Thus, the development of porous structured solar absorbers is highly beneficial for reduced light reflection.

### *3.3. Localized Surface Plasmon Resonance (LSPR)*

Conventional plasmonic metals, such as gold (Au), silver (Ag), and copper (Cu), behave like plasmonic absorbers. Similarly, metallic 2D $Ti_3C_2T_x$ MXenes prevails in its plasmonic resonance feature by absorbing the incident light from visible to the near-IR region [36]. Consequently, the LSPR significantly influences the light-to-heat conversion efficiency, which is ideal during solar desalination. Typically, plasmonic materials greatly absorb the solar light at about 95% and heat the water above the boiling point of water.

### *3.4. Multiple Internal Light Reflection*

To be an effective solar evaporator, the photothermal material should prevail over the pronounced multiple light reflections within the developed specific microstructure. Thus, we should focus on the selective morphology to explain the importance of light-trapping

and multiple light reflections by its inner microstructure. It is to be noted that the unabsorbed light is effectively trapped by the dense surroundings of the microstructure, which eventually creates multiple internal reflections through the reabsorption [37]. Moreover, we can achieve much lower light reflection and higher absorption at a low effective refractive index. The internally reflected light is transmitted through the absorber.

### *3.5. Hydrophilic Nature*

The developed solar absorber should prevail in the high wettable property, which provides persistent water absorption and transportation channel from the bottom toward the surface (top of the absorber) within a short period. Additionally, the hydrophilic nature promotes the heat transfer at the evaporation surface, which strengthens the solar steam generation. In the case of $Ti_3C_2$ MXene, specific surface termination groups (–F, –O, or –OH) provide a hydrophilic nature [38]. This phenomenon is helpful for facilitating the rapid and required water supply through the water transportation channels during the desalination process. On the contrary, hydrophilic materials cannot provide a self-floating property when placed on the water. So, we need to assist additional layers, which reduces the heat conduction toward the bottom layer and provides a self-floating property. It should be noted that hydrophobic structures often yield lower solar evaporation efficiency, compared to hydrophilic structures [39]. Moreover, the hydrophilic wet layer provides more light absorption, compared to the dry layer counterparts.

### *3.6. Light-to-Heat Generation*

The photothermal materials possess an intrinsic light absorption capacity at suppressed light reflection. In such a way, the incident light transforms into thermal energy (heat). Later, the heat evaporates the seawater into freshwater. Compared to the bulk water heating into vapor, interfacial solar heating through the solar absorber inhibits the heat loss toward the water [40]. Eventually, the light-to-heat generation process highlights the desalination of seawater into freshwater. Specific morphological features effectively convert the incident light into heat and strengthen the evaporation rate. Overall, this process should occur at lower heat loss to fulfill the light-to-vapor conversion.

### *3.7. Reduced Salt Blocking or Resistance*

The solar absorber generates the vapor at the interface of the water. On the other hand, salt ions migrate from the surface of the absorber toward the bulk water. The blocking or clogging of salt on the surface of the solar absorber gradually increases the incident light reflection and reduces the water supply channels [41]. Thus, it is necessary to avoid salt blocking on the solar absorber to achieve stable desalination activity throughout the desalination process. On the other hand, we should enable long-term interfacial contact between the seawater and solar absorber (photothermal material) during the desalination process, which defines the salt resistance property. The developing of novel layer structured materials could dissolve the accumulated salt on the solar absorber and diffuse it toward the bulk water.

## 4. Equations Determines the Solar Desalination of Photothermal Material

During the steady desalination process, the following mathematical equations provide in-depth analysis to estimate the efficacy of the developed solar absorbers.

### *4.1. Solar-to-Vapor Conversion Efficiency ($\eta$)*

Effective freshwater production efficiency can be defined as how much solar light is utilized and converted into vapor generation. The solar-to-vapor conversion efficiency ($\eta$) is the key parameter to determine the desalination process, which can be estimated by the following expression [42],

$$\eta = \frac{mh_{LV}}{C_{opt}P_0} \quad (1)$$

where $m$ is the evaporation rate, $h_{LV}$ is the change in the total enthalpy of the liquid-vapor phase, $C_{opt}$ is the optical concentration and $P_0$ is the incident light intensity (1 sun = 100 mW/cm$^2$). In this situation, the evaporation efficiency of developed material should be higher than the natural evaporation rate of pure water.

### *4.2. Photothermal Conversion Ability (E)*

The ability of evaporation rate (E) is quantitatively evaluated by the mass loss of water per unit area in a unit time, using the following equation [43],

$$E = \frac{\Delta_m}{AT} \tag{2}$$

where $A$ is the area of the used container, $\Delta_m$ is the water mass loss and $T$ is the light irradiation time.

### *4.3. Wettability of Photothermal Material*

The wettability or hydrophilic nature (contact angle < 90°) of the developed photothermal material through the effective water flowing channels eventually improves the freshwater generation rate during solar desalination. The wettability can be estimated by the following equation [44],

$$\mathrm{H} = \frac{2\sigma COS\theta}{r\rho g} \tag{3}$$

where $\sigma$ is the surface tension of water, $\rho$ is the density of water, $r$ is the diameter of the channel, $\theta$ is the developed contact angle between water and channel and $g$ is the gravitational constant.

### *4.4. Salt Rejection Ratio*

It is necessary to estimate the salt rejection capability of developed photothermal material, which greatly improves the long-term stability of the desalination process. The salt rejection ($SR$) ratio can be defined as the ratio of salt concentration ($C_{out}$) in the supernatant phase to the initial concentration of saltwater ($C_0$) [45],

$$SR = \frac{C_{out}}{C_0} \times 100\% \tag{4}$$

It is to be noted that $C_{out}$ should be less than $C_0$ after the desalination process, which yields more freshwater generation.

### *4.5. Solar Absorption*

The developed photothermal material should prevail over superior optical absorption throughout the solar spectrum. As a result, we can achieve continuous water evaporation. In such a way, the solar absorption can be evaluated by the following expression [46],

$$\mathrm{A}(\lambda) = 1 - \mathrm{R}(\lambda) - \mathrm{T}(\lambda) \tag{5}$$

where R(λ) and T(λ) are the reflectance and transmittance of the developed sample at different wavelengths (λ). Here, we should obtain an absorption of about 95%, which results from sufficient interaction of light with photothermal material. Eventually, the water evaporation rate can be effectively achieved.

### *4.6. Thermal Conductivity*

The developed solar absorber should prevail low thermal conductivity under minimized heat transfer toward the bulk water. As a result, we can confine the incident light within the surface of the material to achieve more heat generation. In other words, the ma-

terial should prevail over the reduced thermal diffusion heat loss. The following expression gives the conduction loss during solar desalination [47],

$$Q = C m \Delta T \quad (6)$$

where C represents the specific heat of water, $m$ is the water weight, and $\Delta T$ is the improved water temperature within a certain time. Based on this equation, the conduction should be less than 2%, which endows the possible thermal conductive material with freshwater generation.

### *4.7. Evaporation Rate (v)*

The ability of evaporation of the developed solar absorber can be estimated by using the following expression [48]:

$$v = \frac{dm}{Sdt} \quad (7)$$

where $S$ is the resultant surface area of the developed solar absorber and $m$ is the weight of the evaporated fresh water under the specified time ($t$).

## 5. Importance of 2D Materials for Solar Desalination

State-of-the-art 2D materials prevail in their (i) distinct ultrathin morphology, (ii) response to the electromagnetic spectrum, (iii) active surface area, and (iv) hydrophilic nature. These factors guide the cost-effective desalination of seawater into freshwater. It should be noted that graphene, transition metal dichalcogenides (TMDs), and layered double hydroxide (LDH) are reliable for multifunctional applications. Firstly, the 2D material starting with graphene (semi-metallic) can absorb the broad range of the solar spectrum. Later, another 2D material $MoS_2$ raised its importance by providing optical absorption from visible to mid-infrared regions. Here, 2D $MoS_2$ shows a semiconducting-like behavior. Similarly, after the groundbreaking report on 2D material $Ti_3C_2$ MXene by Gogosti et al. [49], $Ti_3C_2$ MXenes were successfully utilized as a photothermal material in the solar desalination process. Nowadays, great interest is continuing for layer structured 2D $Ti_3C_2$ MXenes for freshwater generation. Additionally, the above-mentioned 2D ultrathin layered materials provide a low toxic nature during the water purification process, which is primarily necessary for real-time environmental applications.

## 6. Why 2D $Ti_3C_2$ MXenes for Solar Desalination?

After inventing the layer structured 2D $Ti_3C_2$ MXene in the year 2011 by selective HF etching of aluminum layers in the $Ti_3AlC_2$ MAX phase [49], $Ti_3C_2$ MXenes have been widely used in various applications due to their superior chemical, electrical and mechanical properties. Figure 3 presents the $Ti_3AlC_2$ MAX phase transformation into multilayer and monolayer $Ti_3C_2$ MXene under selective HF etching of Al layers. After realizing the layered morphology, novel 2D $Ti_3C_2$ MXenes were explored for freshwater generation under the solar desalination process by satisfying the following conditions. For achieving stable solar desalination, the material should provide low thermal conductivity and superior photothermal conversion efficiency (PTCE). For this, metallic $Ti_3C_2$ MXene provides localized surface plasmon resonance (LSPR), which paved a potential pathway for the absorption of a wide solar spectrum (250–2500 nm). It should be pointed out that the PTCE and photothermal vaporization capability of $Ti_3C_2$ MXene are 100% and 84%, respectively [50]. Specifically, $Ti_3C_2$ dissipates the absorbed electromagnetic radiation into heat, which is a key factor during the solar desalination process. As a result, multiple internal light reflections occur by the absorption of electromagnetic radiation [13]. On the other hand, $Ti_3C_2$ MXene does not transfer the heat toward bulk water and dissipates the generated heat at the surface. Accordingly, generated heat converts the absorbed water into evaporation. Among all the MXenes, Ti- and C-rich $Ti_3C_2T_x$ MXenes received significant attention in water treatment technology. Remarkably, due to the intrinsic super-hydrophilic nature of $Ti_3C_2$ MXene [51], $Ti_3C_2$ MXene effectively absorbs and transports the bulk water through its water transportation channels. Additionally, $Ti_3C_2$ can recycle after

the water purification process [16]. Through the above light-to-heat conversion efficiency, hydrophilicity, lower thermal conductivity, LSPR, and ideal absorption of broadband, $Ti_3C_2$ MXene raised its ability in freshwater generation and environmental remediation under an eco-friendly solar-driven desalination process.

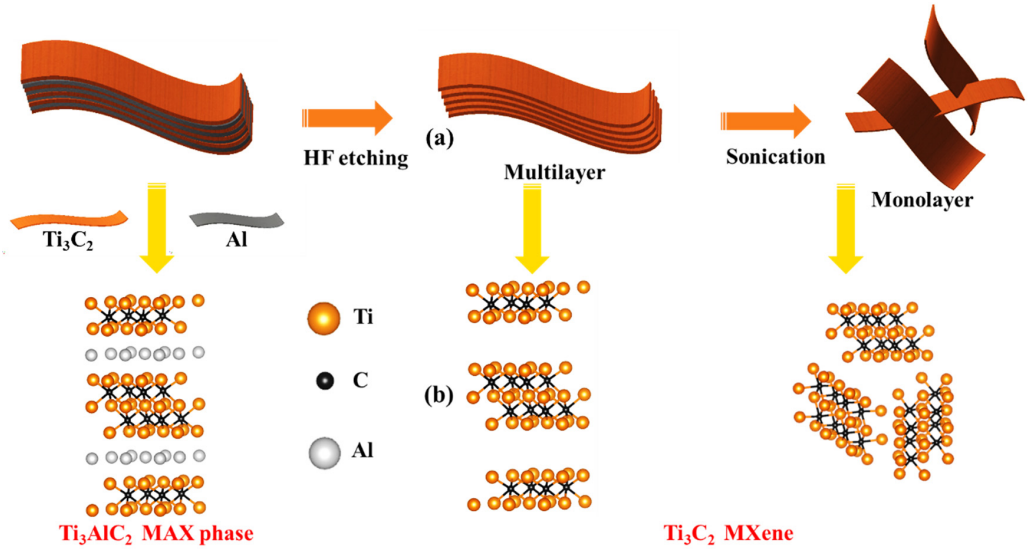


**Figure 3.** (**a**) Schematic representation of HF etching of $Ti_3AlC_2$ MAX phase and its transformation into $Ti_3C_2$ MXene multilayer and monolayer, and (**b**) corresponding chemical bondings in the $Ti_3AlC_2$ MAX phase and $Ti_3C_2$ MXene before and after etching.

## 7. $Ti_3C_2$ MXene-Based Composites

Considering the above constructive features, 2D $Ti_3C_2$ MXene-based composites are greatly dedicated to solar desalination of seawater in the broadband region. However, there is scarce research on solar desalination using 2D $Ti_3C_2$ MXenes. Thus, we addressed the status and ability of $Ti_3C_2$ MXene-based composites toward solar desalination by highlighting its intrinsic photothermal conversion under ideal light consumption, water absorption, and hydrophilic nature. Specifically, we explored the importance of various morphological features of $Ti_3C_2$ MXenes for seawater absorption and desalination. Thus, we provided the proof-of-concept of $Ti_3C_2$ MXenes in the form of aerogel, films, foam, hydrogel, membrane, monolith, and porous structures to reveal the importance of light absorption capacity and light-to-heat generation for efficient solar desalination and freshwater generation.

### *7.1. Aerogel*

Aerogels prevail in their abundant porous network, low thermal conductivity, hydrophilic nature, and low mass density. Thus, the aerogels morphology is highly beneficial for solar thermal evaporation [52]. Specifically, aerogel features can be successfully achieved by 2D $Ti_3C_2$ MXenes, which can effectively apply in the solar desalination process.

Ming et al. [53] successfully developed the multilevel porous structured aerogel by integrating the 2D $Ti_3C_2T_x$ MXene and 3D graphene oxide (GO), which can weigh 500 times (500 g) higher than its own weight. Mainly, they explored heat localization, photothermal ability, solar-driven interfacial water evaporation in complex conditions (including summer and winter). For this, various MXene to GO (GMA) (1:1, 1:3, and 1:5) ratios were developed. Under constructive interfacial interaction between GO and $Ti_3C_2T_x$, self-enhanced photothermal conversion was achieved through heat localization on the top of the layer. The role of GO in the multilevel GMA aerogel was to prevent the oxidization and restacking of $Ti_3C_2T_x$ MXene, which results in the synergy between GO and $Ti_3C_2T_x$ MXene. Optimized GMA-3 (1:3) aerogel is satisfied with a hydrophilic nature, which is highly beneficial for rapid water absorption and transportation. It should be noted that the resultant GMA aerogel exhibited an ultra-lightweight feature due to the prominent

multilevel porous structure. Figure 4a shows the digital image and morphology of GMA-3 during water evaporation and the microstructure with the internal gap, micron channels, and nano wrinkles for achieving interfacial evaporation. In such a way, GMA-3 achieved an evaporation efficiency of about ~90.7% at the evaporation rate of 1.27 kg/m$^2$h under 1 sun, compared to GO aerosol (~63.7% and 0.88 kg/m$^2$h) and $Ti_3C_2T_x$ MXene (~71.4% and 1.02 kg/m$^2$h). Due to the high thermal conduction of GO, the top portion of the GMA-3 aerogel generated heat, which converted into evaporation. Consequently, the sharp rise in the surface temperature (41.9 °C in 300 s) was observed. The resultant GMA composite achieved excellent photothermal activity by satisfying the self-reduction/oxidation between GO and $Ti_3C_2T_x$ MXene compared to pure GO and MXene. Interestingly, the internal light reflection, interfacial evaporation, and low thermal conductivity were predominately observed during the desalination process as shown in Figure 4b. Finally, the solar-driven interfacial evaporation process was highlighted through the (i) interfacial evaporation (~90.7%), (ii) lower thermal radiation (~3.42%), (iii) lower thermal convection (~2.50%), and (iv) lower heat convection (~1.50%). These factors motivated the development of a prototype for freshwater generation (Figure 4c). In comparison, solar evaporation during summer (1.27 kg/m$^2$h) is higher compared to the winter season (0.73 kg/m$^2$h) under peak sunlight (12:00 a.m. to 14:00 p.m.). Under these conditions, the GMA-3 was observed with 24 h stability.

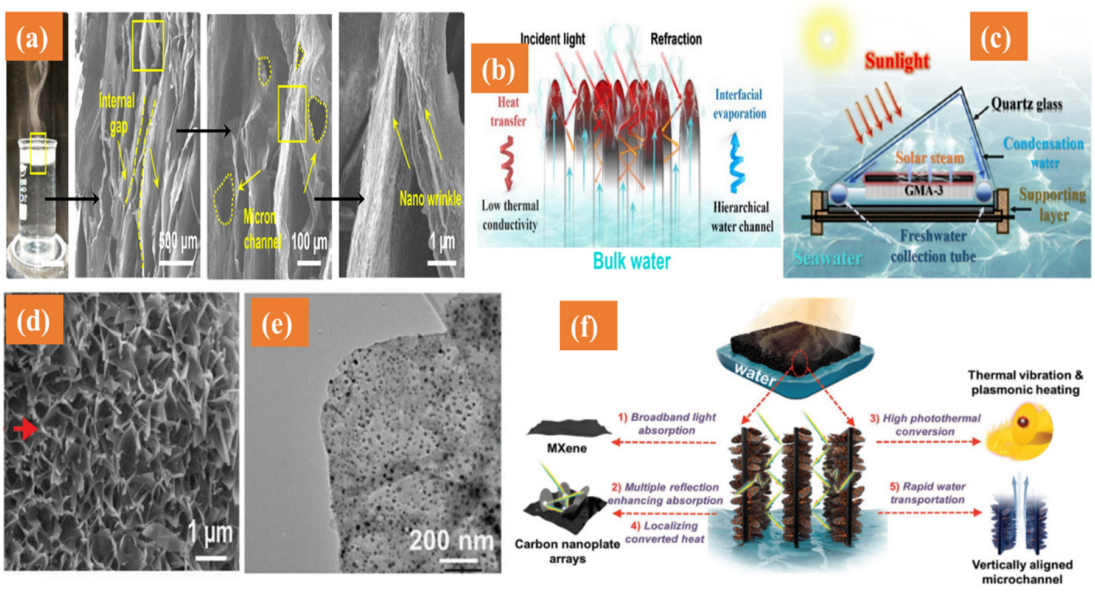


**Figure 4.** (**a**) Internal gap, microchannels, and nano wrinkles developed on the internal surface of GO supported $Ti_3C_2$ MXene aerogels for water supplying channels during solar desalination, (**b**) internal light refraction for superior light absorption and heat localization for interfacial evaporation at low thermal conductivity, and (**c**) schematic representation of solar desalination process by the GMA-3 (reprinted from Ref. [53], copyright with permission from Elsevier, 2020), (**d**) magnified SEM image of 3D $Ti_3C_2$ MXene nanosheets supported hierarchical cobalt nanoparticle–carbonaceous nanosheets/MXene foam, (**e**) corresponding TEM image with Co nanoparticles within the Co-CNS/M foam, and (**f**) key features which improved the solar desalination of Co-CNS/M foam. (Reprinted from Ref. [17], copyright with permission from Wiley Online Library, 2020).

Besides sunny days, it is necessary to achieve steam generation in all weather conditions and any complex environments. Thus, a strategic combination of photothermal and electro-thermal conversion effects is highly beneficial for all-weather steam generation. Specifically, during sunny days, batteries can store the electrical energy, which will be utilized for electro-thermal steam generation under low light and dark conditions. For this, Zaho et al. [15] strategically explored the groundbreaking report on continuous steam generation in complex environments (strong sunlight, weak light, and no light conditions) by developing the cross-linked MXene aerogel (CMA). The CMA was developed by assembling the GO with $Ti_3C_2T_x$ MXene (co-gelation strategy) at an optimized MXene content

of 90% (CMA-90%). The cross-linked MXene aerogel loaded 1040 g, which is higher than previously reported GO-supported $Ti_3C_2$ MXene aerogel (500 g) [53]. Here, GO played a crucial role in assembling $Ti_3C_2T_x$ MXene nanosheets into crosslinked aerogels. It is to be noted that $Ti_3C_2$ MXene prevailed over LSPR for photo-thermal conversion of conventional plasmonic metals (Au and Ag). As a result, the light absorption capacity of CMA-90% is 99%. The surface temperature of aerogel changed from 80° (at an incident angle of 30°) to 235 °C with the increase in solar irradiation from 1 $kWm^{-2}$ to 5 $kWm^{-2}$ respectively, which suggests the superior photothermal conversion capability of CMA aerogel. The CMA sample prevailed as superior in its hydrophilic nature, which supported water absorption and transportation ability. In addition to photothermal conversion, CMA revealed the electro-thermal conversion ability. It should be noted that simultaneous electrical energy and solar illumination effects prevail in their increase in the surface temperature and reduced humidity of the overall system, respectively. Under both conditions (photothermal + electro-thermal) at a weak solar light intensity of 0.5 $kWm^{-2}$ and electric supply of 2.5 V, CMA-90% achieved a superior evaporation rate of 1.624 $kg/m^2h$ and energy conversion efficiency of 88.4%, which is higher than the sole 1 sun solar light (1.337 $kg/m^2h$ and ~85%). CMA-90% aerogel achieved superior electrical conductivity, compared to the conventional graphene aerogel and carbon nanotube foam. Overall, a strategic combination of photothermal and electro-thermal effects was successfully studied by the $Ti_3C_2T_x$ MXene-based aerogel for the all-weather solar desalination process.

In another study, vertically aligned two-layer (hydrophobic/hydrophilic interface) Janus $Ti_3C_2$ MXene aerogel (VA-MXA) was developed for revealing the solar desalination process [54]. The specific features of the vertically aligned Janus $Ti_3C_2$ MXene succeeded the desalination process with a prominent (i) capillary water transport channel, (ii) light absorption capacity, (iii) multiple internal light reflection, and (iv) vapor escape ability compared to conventional MXene and Janus MXene. Specifically, the top layer provided a superior hydrophobic nature with a contact angle of 133.2° and the bottom layer acted as a hydrophilic surface (46.2°). The top layer benefited from the light absorption, heat confinement, reduced heat loss, and salt rejection by retaining salt ions from the bottom (hydrophilic surface), whereas the submerged bottom hydrophilic surface effectively pumped the water toward the top layer, where solar steam production occurred. Under these well-ordered features, they avoided the crystallization of salt on the absorber for improvement in the water evaporation. Interestingly, stable steam generation was observed at the air–water interface. The selective VA-$MXA_{15}$ aerogel with microchannel size of 15 μm (at $Ti_3C_2$-25 mg. $mL^{-1}$) achieved an energy conversion efficiency of ~87% and evaporation rate of 1.46 $kg/m^2h$ (without any absorber-0.49 $kg/m^2h$) for 15 days under 1 sun following the LSPR [55]. The incident light (200–2500 nm) absorption capacity was maintained at about 96% after 12 h. Additionally, the scalable freshwater yield of ~6 L $m^{-2}$ was achieved. The average surface temperature increased from 21.3 °C to 59.4 °C within 300 s. Here, the central part of the VA-$MXA_{15}$ aerogel achieved 98.5 °C compared to the bottom portion (29.4 °C), which suggested that the top layer of VA-MXA localized the generated heat and did not transfer toward the bottom following the heat localization effect and lower thermal conductivity. Thus, the hydrophobic/hydrophilic interface effectively confined the generated heat. Additionally, they mainly overcame the crystallization of saltwater on the absorber to prevail in stable freshwater production. Overall, vertically aligned Janus $Ti_3C_2$ MXene aerogel under opposite wettable conditions, heat localization, salt rejection, and improved light-to-heat conversion guided a new concept of freshwater generation.

Of these aerogels designed by the 2D $Ti_3C_2$ MXenes, the superior hydrophilic nature guided effective water transportation channels for water absorption and photothermal activity at low thermal conductivity. The improved solar absorption and multiple light reflection within the MXene aerogels contributed through the intrinsic LSPR property of $Ti_3C_2$ MXene. Specifically, 2D $Ti_3C_2$ MXenes aerogels contributed to their desalination performance in all-weather conditions, which proved the environmental viability of $Ti_3C_2$ MXene. Additionally, $Ti_3C_2$ MXene achieved good salt-resistance activity when it interacted

with seawater during the desalination process. The salt resistance activity of the developed solar absorber provided long-term interfacial interaction with seawater.

### *7.2. Foam*

As we mentioned before, incident light reflects and blocks water transportation channels due to salt blocking during the seawater desalination process. Thus, we should conquer the salt blocking ability and broadband absorption for continuous freshwater generation with high efficiency. For this, Fan et al. [17] combined the 3D $Ti_3C_2$ MXene nanosheets and cobalt-based metal-organic frameworks (Co-MOFs) as precursors for designing the hierarchical cobalt nanoparticle-carbonaceous nanosheets/MXene foam (Co-CNS/M foam). Here, the Co-MOF nanosheets are embedded with Co nanoparticles, which are vertically aligned on the MXene (Figure 4d,e). The vertically aligned microchannels in the foam exhibited a width of about 30–50 µm. The microchannel wall in MXene-based foam was observed with a lamellar structure. By developing these hierarchical structures, the following interesting features were observed: (i) multiple light reflection by the carbon nanoplate arrays and Co nanoparticles for improved light absorption, (ii) improved light-to-heat conversion by the thermal vibration of molecules and plasmonic localized heating, (iii) carbon nanoplate arrays on the MXene skeleton for reduced thermal conductivity and chemical stability for heat loss, (iv) broadband absorption of up to 2500 nm by the MXene nanosheets and carbon nanosheets, and (v) hydrophilic nature for enabling the water transportation channel. All these constructive features significantly improved the salt-rejection capacity throughout the solar desalination process as shown in Figure 4 (f). Specifically, Co-CNS/M foam revealed a thermal conductivity about 0.242 $Wm^{-1}K^{-1}$, which is less than pure MXene (0.345 $Wm^{-1}K^{-1}$) due to the localization of heat. These factors suggest that amorphous carbon nanoplates developed on MXene and the existence of a hierarchical porous architecture. The Co-CNS/M foam achieved superior solar absorbance of about 97.5% compared to pure MXene foam, (95%) up to 2000 nm. Most importantly, the surface temperature of Co-CNS/M was about 69.8°C within 1 min. Overall, Co-CNS/M foam achieved solar to thermal conversion efficiency at an average of 93.06% under 1 sun for 10 days (10 h per day) with a water evaporation rate of 1.393 $kg/m^2h$, compared to pure MXene-1.306 $kg/m^2h$.

### *7.3. Hydrogel*

Hydrogels can hold water multiple times higher than its weight [56]. Considering this point, MXene-based photothermal hydrogels were developed for multifunctional solar water purification (photothermal) and the degradation of contaminants. Fan et al. [18] developed the mixed-dimensional $Ti_3C_2T_x$ MXene-based nanohetero structures ($Ti_3C_2T_x$/$La_{0.5}Sr_{0.5}CoO_3$ (MLH)) for promoting solar water evaporation under excellent thermal insulation. Here, a facile hydrothermal reaction process was adopted to attach the 0D $La_{0.5}Sr_{0.5}CoO_3$ nanoparticles on $Ti_3C_2T_x$ MXene. Figure 5a,b shows the TEM image and interfacial interaction between $Ti_3C_2T_x$ MXene nanosheets (blue line) and $La_{0.5}Sr_{0.5}CoO_3$ nanoparticles (green lines). Selective weight ratio between $Ti_3C_2T_x$ MXene and LSC at 1:10 (MLH-2) yielded fruitful evaporation rate of 2.73 $kg/m^2h$, which was higher than pure water (0.55 $kg/m^2h$), MXene (2.26 $kg/m^2h$), and $La_{0.5}Sr_{0.5}CoO_3$ (2.24 $kg/m^2h$) with superior evaporation efficiency of 92.3% under 1 sun and average solar absorption (250–2500 nm) of 94.1% as shown in Figure 5c. Specifically, the MLH-2 hydrogel exhibited a microporous skeleton structure. At this condition, the saturated water content significantly increased within 60 s, which suggests the hydrophilic nature. The ability of cross-linked hydrogels was evaluated by measuring the mechanical stability, which suggested a higher storage modulus than loss modulus. It should be noted that the developed composite included negligible heat convection (~1.40%), radiation (~2.28%), and conduction (~0.8%), which supported improvement in the evaporation efficiency. The solar evaporation system designed based on the $Ti_3C_2T_x/La_{0.5}Sr_{0.5}CoO_3$ hydrogel is shown in Figure 5d. The low energy distribution of MLH-2 hydrogel with an enthalpy of 1175 J $g^{-1}$ was observed com-

pared to pure water (2250 J $g^{-1}$), which suggests efficient evaporation ability. Overall, the low thermal conduction ability of $Ti_3C_2T_x/La_{0.5}Sr_{0.5}CoO_3$ composite extensively absorbed the wide spectrum of solar light and saturated the water content in a shorter time, for achieving stable solar desalination process. The efficient mechanical and water storage capacity of the hydrogels suggests its importance in practical solar desalination of seawater into freshwater. Table 1 presents the solar desalination activity of $Ti_3C_2$ MXene-based aerogel, foam, and hydrogel morphologies.

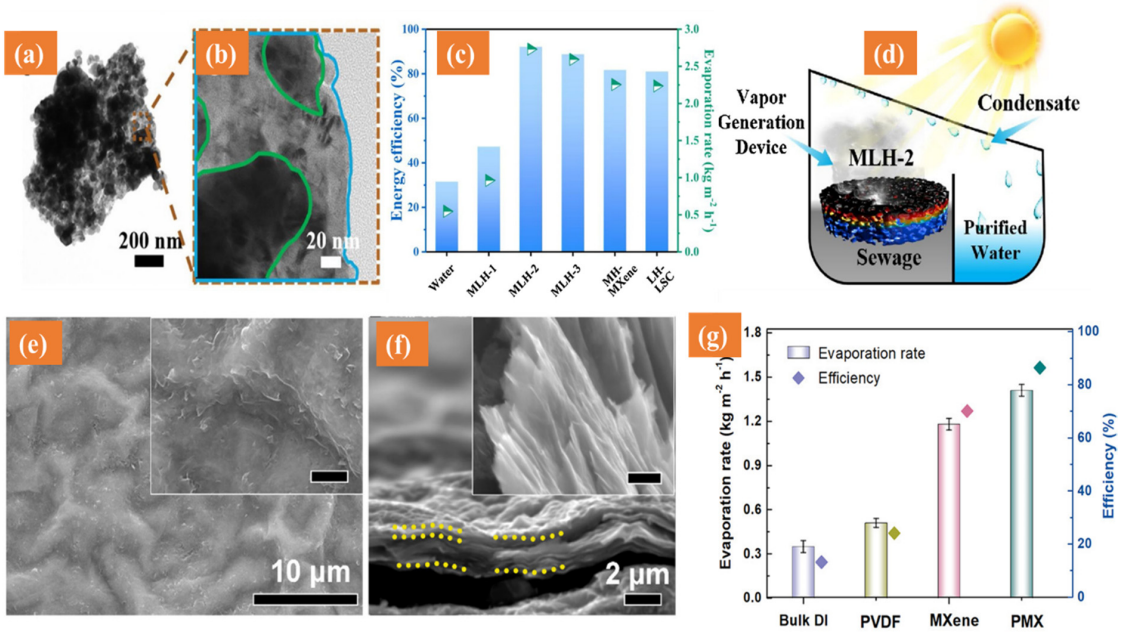


**Figure 5.** (**a**,**b**) TEM image and interfacial interaction between $Ti_3C_2T_x$ MXene nanosheets (blue line) and $La_{0.5}Sr_{0.5}CoO_3$ nanoparticles (green lines), (**c**) evaporation efficiency of $Ti_3C_2T_x$ MXene and $La_{0.5}Sr_{0.5}CoO_3$ at different weight ratios, and (**d**) designed prototype of solar-driven sewage purification system (Reprinted from Ref. [18], copyright with permission from Elsevier, 2021), (**e**,**f**) top and cross-section view of Janus PMX membrane, and (**g**) evaporation rate and efficiency of Janus PMX membrane compared to base components (reprinted from Ref. [57], copyright with permission from American Chemical Society, 2021).

**Table 1.** Summary of $Ti_3C_2$-based aerogel, foam and hydrogel morphologies for solar desalination.

| $Ti_3C_2$-Based Aerogel, Foam and Hydrogel Morphologies for Solar Desalination | | | | | | | |
|---|---|---|---|---|---|---|---|
| **$Ti_3C_2$-Based Composite (Optimized Condition)** | **$Ti_3C_2$ Functional Groups (Etching Process)** | **Solar Evaporation Efficiency (%) (1 Sun)** | **Surface Temperature (°C)** | **Stability** | **Solar Desalination Rate ($Kg/m^2h$)** | | **Ref.** |
| | | | | | **Base Material** | **Resultant Composite** | |
| **Aerogel** | | | | | | | |
| **GO/$Ti_3C_2T_x$ (MXene to GO-1:3)** | O, OH and/or F (HCl and LiF) | ~90.7 | ~41.9 | 24 h (acid and alkaline environment) | GO-0.88, $Ti_3C_2T_x$-1.02 | 1.27 | [53] |
| **GO/$Ti_3C_2T_x$ ($Ti_3C_2T_x$-90%)** | O, OH, and F (HCl and LiF) | ~85.0 | 80 | — | — | 1.337 | [15] |
| **$Ti_3C_2$ (Micro-channel size of 15 μm (at $Ti_3C_2$-25 $mg.mL^{-1}$)** | — | 87 | 59.4 (300 s) | 15 days (sea water) | — | 1.46 | [54] |
| **Foam** | | | | | | | |
| **Cobalt nanoparticle-carbonaceous nanosheets/MXene** | HCl and LiF | 93.06 | 69.8 (60 s) | 10 days | MXene foam-1.306 | 1.393 | [17] |
| **Hydrogel** | | | | | | | |
| **$Ti_3C_2T_x/La_{0.5}Sr_{0.5}CoO_3$ (Weight ratio of MXene to $La_{0.5}Sr_{0.5}CoO_3$-1:10)** | $NH_4F$ and HCl | 92.3 | 40 (10 min) | 10 cycles (Each cycle 60 min) | $Ti_3C_2T_x$-2.26, $La_{0.5}Sr_{0.5}CoO_3$-2.24 | 2.73 | [18] |

### *7.4. Membrane*

Membrane-based water purification technology plays a significant role in producing fresh drinking water from seawater and wastewater. Nowadays, MXene-based composites in the form of the membrane have received much attention for solar desalination. Thus, we plan to reveal the ability of MXene-based composite membranes for freshwater generation, which are practically applicable in the development of advanced water treatment technologies. In this manner, various researchers particularly focused on $Ti_3C_2$ MXene membrane-related composites to achieve significant water purification.

During the desalination process, the salt blocking activity of the developed absorber plays a key role to achieve stable freshwater production. Generally, $Ti_3C_2$ MXene prevails in its superior hydrophilic nature and intrinsic light-to-heat conversion ability [39]. In contrast, the hydrophobic surface enables the salt-bocking feature on delaminated $Ti_3C_2$ MXene (10 mg) nanosheet membrane compared to the hydrophilic surface for efficient solar desalination [58]. Thus, they compared the desalination efficiency of the hydrophobic surface with hydrophilic membranes. Here, the hydrophobic $Ti_3C_2$ MXene membrane was achieved following the vacuum filtration method of Ding et al. [19]. It should be noted that hydrophobic delaminated $Ti_3C_2$ MXene successfully blocked the salt compared to the hydrophilic surface. The salt blocking strategy and hydrophobic nature of the -OH terminated $Ti_3C_2$ MXene membrane was effectively achieved by the addition of trimethoxy (1H,1H,2H,2H-per-fuorodecyl) silane (PFDTMS). These features are utilized for the development of commercial water filter membranes. Here, PFDTMS completely transformed the hydrophilic $Ti_3C_2$ MXene into a hydrophobic nature. In such a way, pure $Ti_3C_2$ MXene prevailed over the hydrophilic nature at a water contact angle of 38.8°. However, the PFDTMS-modified $Ti_3C_2$ MXene surface provided the hydrophobic nature with a water contact angle of 102.0°. The $Ti_3C_2$ MXene surface was covered with -$CF_3$ groups for achieving a hydrophilic nature. During the solar desalination process, the membrane gained a vapor temperature about 39 °C within 5–10 min. Due to the non-wettable feature of the $Ti_3C_2$ MXene surface, the developed heat effectively localized on the surface without transferring toward the bulk water. Under these strange surface features, the hydrophobic $Ti_3C_2$ MXene membrane achieved an evaporation rate of 1.31 kg/$m^2$h (pure seawater-0.42 kg/$m^2$h) with steam conversion efficiency of 71% and seawater desalination rate of 99.5% for 200 h under 1 sun. The conventional hydrophilic $Ti_3C_2$ MXene membrane achieved an evaporation rate of 1.41 kg/$m^2$h at a steam conversion efficiency of 74%. Additionally, negligible natural evaporation of about 0.19 kg/$m^2$h was also observed under a dark state due to the hydrophobic nature of the membrane. Overall, the hydrophilic membranes prevailed as the key feature of the salt blocking ability for the efficient and long-term solar desalination of seawater into freshwater.

In addition to the salt blocking, we should reduce the incident light reflection to improve the solar steam generation. In such a way, the first-time deformation of the hierarchical $Ti_3C_2T_x$ MXene ($G_1$) nanocoatings into a crumpled morphology succeeded for broadband light absorption [59]. In this study, they mainly highlighted the bioinspired $Ti_3C_2T_x$ MXene crumpled structures (such as West African Gaboon Viper), which strongly scattered and reflected the incident light multiple times within the MXene. Consequently, a superior light-to-heat phenomenon was observed. Specifically, broadband absorption (up to 2500 nm) was achieved under an improved equilibrium temperature. Additionally, improvement in the light absorption and decreased reflectance were successfully achieved. Such biomimetic $Ti_3C_2T_x$ MXene morphological features significantly achieved an evaporation rate of 1.33 kg/$m^2$h under 1 sun with broadband absorption up to 93.2% at a lower solar thermal loading of 0.32 mg $cm^{-2}$. The hydrophilic nature of MXene was also highlighted during the water supply process. Moreover, the $Ti_3C_2T_x$ MXene converted the incident light into heat at about 65.4°C. The planar MXene morphology was observed with reduced light absorption (46.8–64.0%) and light-to-heat generation (50.4–58.1 °C) compared to the crumpled morphology. Finally, mechanically deformed $Ti_3C_2T_x$ MXenes prevailed with the following prominent features: (i) thermal insulation, (ii) mechanical stretchability,

(iii) increased light absorption by scattering, (iv) multiple incident light reflection within the MXene, (v) negligible transmittance, and (vi) low reflection. On the other hand, bioinspired $Ti_3C_2T_x$ MXene features suggested the formation of novel stretchable solar steam generation devices.

As we discussed before, we need to conquer the light reflection losses and salt resistance at the interface of the solar absorber and liquid. In this manner, we can improve the incident light absorption capacity by the photothermal 2D materials. For this, Wang et al. [60] developed the $Cu_3BiS_3$ (CBS) on $Ti_3C_2$ MXene nanosheets (0.2 g) for the first time via the thermal-injection method in the ratio of 1:1 (CBS-$Ti_3C_2$). Later, this composition at different loadings (0.12, 0.24, 0.48, and 0.60 mg $cm^{-2}$) was placed on a hydrophilic porous filter membrane (PVDF) and vacuum dried overnight. As a result, the coatings were strongly attached to the PVDF membrane during the desalination process. Accordon-like $Ti_3C_2$ transformed into improved porosity and specific surface area in the CBS–$Ti_3C_2$ composite. These morphological features proved to have rapid water transportation channels and avoided the formation of high saltwater areas. Accordingly, the CBS–$Ti_3C_2$ (0.48 mg $cm^{-2}$) composite revealed steady light-to-heat generation of about 62.3°C (at 0° incident angle), which is higher than that of pure $Ti_3C_2$ (53.8°C). In such a way, CBS–$Ti_3C_2$ achieved superior photothermal evaporation efficiency of 91.9% under 1 sun, which is higher than other light intensities (3 sun—88.2%, and 5 sun—90.2%). The main -OH termination groups transformed into -O in the CBS–$Ti_3C_2$ compared to pure $Ti_3C_2$ under the unchanged chemical state of $Ti_3C_2$. These results suggest the efficient light-to-heat conversion ability of CBS–$Ti_3C_2$. In the same manner, CBS–$Ti_3C_2$ yielded an evaporation rate of 1.32 kg/$m^2$h (1 sun), 3.84 kg/$m^2$h (3 sun) and 6.26 kg/$m^2$h (5 sun) in 60 min. Due to the combination of the high absorption coefficient of $Ti_3C_2$ in the visible region and $Cu_3BiS_3$ in the near-infrared region, the solar light absorption capacity of CBS–$Ti_3C_2$ (0.48 mg $cm^{-2}$) was about 87.11% in the range of 300–2500 nm, which is higher than CBS–$Ti_3C_2$ at 0.12 mg $cm^{-2}$ (85.56%).

In another study, the light-to-heat conversion efficiency of 100% was achieved on a self-floating 2D $Ti_3C_2$ MXene thin film membrane [39]. In this study, the light-to-heat conversion efficiency was revealed by the droplet laser heating process. During the experiment, the droplet temperature was accurately measured by a precalibrated IR camera. An aqueous droplet of $Ti_3C_2$ MXene (0.1 mg/mL) with 9.0 μL hung at the end of the PTFE pipet. Here, monochromatic wavelengths of 473 nm and 785 nm were illuminated at a power density of 82 mW and spot size of 0.85 nm in diameter. The laser point perfectly focused on the center of the droplet. During the light-to-heat conversion process, incident light energy was significantly absorbed by the MXene sheets and converted into heat. The scattered light is partially absorbed by the $Ti_3C_2$ MXene, which does not directly interact with the laser beam. During the water droplet evaporation, the droplet volume was slightly shrunken by about 0.2 mm. On the other hand, a certain amount of heat energy is converted into internal energy in the droplet system. Here, the heat energy gained by the MXene droplet was equal to the heat energy dissipation at equilibrium condition, which maintained the droplet temperatures constantly, compared to the carbon nanotubes. Thus, MXene sheets achieved a light-to-heat conversion efficiency of 100%. On the other hand, the self-floating nature, mechanical strength, and light-to-water evaporation efficiency were achieved by the interaction of MXene with the hydrophilic PVDF photothermal membrane (0.22 μm). The developed MXenes could be peeled off from the PVDF to create a self-floating activity. To decrease the surface energy and hydrophilic nature of MXene–PVDF, PDMS was grafted on MXene–PVDF to self-float on top of the water. The MXene–PVDF membrane achieved an equilibrium temperature of about 75°C (PVDF 30 °C). The PDMS maintained negligible light absorption and reflection of the membranes. Generally, superior water steam generation can be achieved under higher surface temperatures. In this situation, a light-to-water evaporation efficiency of 84% was achieved by the MXene sheets under one sun irradiation.

Very recently, Zhao et al. [61], for the first time, reported the self-assembly of 0D polydopamine microsphere (PDA) and 2D $Ti_3C_2$ MXene flakes (PDA@MXene microsphere)

to realize the broadband light absorption capacity (250–1500 nm). The PDA@MXene microsphere was developed on a hydrophilic PVDF membrane. This composite prevailed with folding, refolding, and recovering features. The presence of -OH, -F, and -O termination groups on the $Ti_3C_2$ MXene created the negative charge. Specifically, key features, such as (i) reduced light reflection, (ii) minimized heat conduction towards bulk water, and (iii) convention and radiation losses were explored. Additionally, the PDA@MXene achieved rapid water transportation toward the surface and heat localization, compared to the PDA/MXene. Most importantly, PDA@MXene composite achieved a surface temperature of 80 °C, which enlightened the photothermal conversion capability under a stable light absorption capacity of 96%. Accordingly, the selective hydrophilic PDA@MXene (0.8 mg/cm$^2$) membrane composite succeeded the water evaporation ratio (1.276 kg/m$^2$h), solar-to-vapor conversion efficiency (85.2%), and salt rejection rate beyond 99%. These values are higher than those of pure PDA (1.157 kg/m$^2$h) and $Ti_3C_2$ MXene (1.095 kg/m$^2$h) under 1 sun. The oxidation stability and light absorption stability of the PDA@MXene membrane were also studied, which revealed no oxidation peaks ($TiO_2$) after 50 h of aging. Eventually, the PDA@MXene membrane was highlighted with significant light absorption capacity and negligible oxidation during solar desalination for efficient freshwater generation.

During the desalination process, we should mainly focus on the hydrophilic nature of the developed photothermal material. In contrast, Zhang et al. [57] developed a stable hydrophobic/hydrophilic fluorinated porphyrin–$Ti_3C_2T_x$ MXene (PMX) Janus membrane to reveal the superior photothermal desalination. Mainly, they addressed the good salt-resistance performance. Figure 5e,f presents the top and cross-sectional views of the PMX membrane. Previously, a vertically aligned Janus $Ti_3C_2$ MXene aerogel was also studied based on the hydrophobic/hydrophilic phenomena, which benefited multiple light reflections at an evaporation rate of 1.46 kg/m$^2$h [54]. The upper surface of the hydrophobic/hydrophilic Janus PMX membrane made a water contact angle of 143.9° (fluorinated porphyrin) and the bottom layer made one of a hydrophilic nature (72°). Among these, the hydrophobic surface greatly benefited the heat localization and salt resistance. Such a salt-blocking feature was also observed on the $Ti_3C_2$ MXene surface with a hydrophobic nature of 102.0° [58], whereas hydrophilic $Ti_3C_2T_x$ MXene effectively pumped the water toward the hot interface. As a result, the resultant PMX membrane contributed efficient vapor generation under 1 sun by generating a surface temperature of about 66.0 °C, which is higher than that of the pure MXene membrane (43.2 °C). Overall, the PMX Janus membrane achieved a stable photothermal evaporation rate of about 1.41 ± 0.04 kg/m$^2$h with an evaporation rate of 86.4% (Figure 5g). These results are almost similar to the previously studied another form of the Janus $Ti_3C_2$ MXene aerogel [54].

Similar to the PVDF membrane interfacial interaction with the $Ti_3C_2$ MXene [39,60,61], another study on the $Ti_3C_2$/PVDF membrane was explored by Peng et al. [62]. They revealed an efficient air–water interface during solar desalination. In this study, the $Ti_3C_2$/PVDF membrane achieved a hydrophobic nature with a water contact angle of 128.6°, which benefited the floating of the $Ti_3C_2$/PVDF membrane (light-absorbing material) on water due to surface tension. Here, they highlighted the air–water interface activity of $Ti_3C_2$ MXene under a superior solar absorption efficiency of 96.36%. In such a way, the surface temperature of the $Ti_3C_2$/PVDF membrane achieved 43.3 °C in 10 min after solar light illumination (48 °C, 1 h). This value was 11.8 °C higher than pure water. It should be noted that the temperature at the air–water interface without light condition was 21.2 °C. The difference in the temperature confirms the light-to-heat conversion effect by the self-floating $Ti_3C_2$/PVDF membrane. Specifically, $Ti_3C_2$ MXene is suitable for the heat absorption and air–water interface heating effect. The selective $Ti_3C_2$ content of 60 mg in $Ti_3C_2$/PVDF achieved an evaporation rate of 0.98 kg/m$^2$h (pure water, 0.35 kg/m$^2$h) under 2 sun and stable for 30 days. At this condition, the water evaporation rate was 0.01633 kg/m$^2$min. At a higher $Ti_3C_2$ content (70 mg), a decrement in the evaporation rate was observed (0.89 kg/m$^2$h) due to the suppressed vapor transport velocity of excessive $Ti_3C_2$.

The above $Ti_3C_2$ membrane-based composites effectively explained the self-floating nature and salt-blocking effect for boosting the sweater desalination activity. Specifically, the internal light reflection and hydrophobic nature of the top layer significantly increased the light-to-heat generation and localization of heat for efficient water evaporation. Thus, the $Ti_3C_2$ membrane-based composites paved a potential path toward freshwater generation.

### *7.5. Monoliths*

In addition to the solar desalination (photothermal effect), voltage difference (Seebeck effect) was also explored through the temperature difference between the top and bottom layer of the absorber under solar light. This phenomenon can be explained as the light-to-heat-to-electricity effect. Following the above concept, Zhang et al. [20] realized the novel temperature difference–induced electricity by the combination of the bilayer $Ti_3C_2$ MXene-based monolith (B-MXM) (hydrophobic and hydrophilic) with n- and p-type silicon slices. In this study, the bottom portion of $Ti_3C_2$ MXene submerged in water prevailed with a stable hydrophilic nature and a water contact angle of 43.5°, which continuously led to the rapid dissociation of salt and avoided salt crystallization. The hydrophobic nature of the $Ti_3C_2$ MXene upper layer localized the heat as shown in Figure 6a. Zhang et al. [57] also reported such a hydrophobic/hydrophilic phenomenon on the $Ti_3C_2T_x$ MXene Janus membrane for solar desalination. The upper hydrophobic surface layer generated a temperature of about 98 °C than the lower B-MXM surface (30 °C), which suggests that heat effectively localized on the top of the surface. Consequently, thermal conduction was reduced toward the bulk water. Accordingly, B-MXM achieved an evaporation rate of about 1.39 kg/$m^2$h under outdoor natural sunlight (0.91 $kWm^{-2}$) with a solar thermal efficiency of ~82.9% and sustained voltage of ~0.3 V in the afternoon 12:00 p.m. (noon) as shown in Figure 6b. It should be noted that this study further elevated the light-to-heat concept into light-to-heat-to-electricity. Figure 6c presents the simultaneous solar desalination and voltage measurements, using hydrophobic and hydrophilic mediated B-MXM composites.

### *7.6. Porous*

$Ti_3C_2$ MXenes in the form of tightly packed 2D membranes create high reflection losses and restrict the water from flowing, which suppresses the overall evaporation rate. To overcome this, macroporous 3D $Ti_3C_2$ MXene interfaced carbonized melamine foam (CMF@d-$Ti_3C_2$) was developed for improving the rapid flow of water and escaping the water vapor [63]. In this study, CMF@d–$Ti_3C_2$ was used as a solar absorber and evaporator. For floating the porous CMF@d–$Ti_3C_2$ composite, thermal insulated polystyrene foam was used. For water transportation under the capillary effect, nonwoven fabric was used. The 2D to 3D morphologic transformation of $Ti_3C_2$ in the resultant porous structured CMF@d–$Ti_3C_2$ elongated the optical path and improved the absorption of incident solar light. Additionally, CMF@d–$Ti_3C_2$ sustained an excellent hydrophilic nature. The absorber temperature gradually reached 40 °C after 10 min with a vapor temperature of 42 °C. The porous surface of the CMF@d–$Ti_3C_2$ composite greatly reduced the specular reflection losses. Under these constructive 3D architectures, CMF@d–$Ti_3C_2$ significantly achieved an evaporation rate of 1.60 kg/$m^2$h, which is higher than that of 2D $Ti_3C_2$ (1.41 kg/$m^2$h), with thermal evaporation efficiency of 84.6% (13 h) under 1 sun.

In a similar way, the morphological transformation of 2D $Ti_3C_2T_x$ into 3D was successfully explored for the solar desalination activity under strategic self-floating and direct contact with bulk water [21]. Here, the microporous hydrophilic 3D $Ti_3C_2T_x$ MXene architecture (3DMA) was developed on the melamine foam (MF) skeleton under the adhesion force of PVA. The strong capillary effect was observed by the hydrophilic 3DMA and MF. Specifically, continuous water flow was observed from MF to 3DMA. Moreover, the 2D to 3D morphological evolution of $Ti_3C_2T_x$ MXene significantly improved the light absorption capacity from the UV to NIR region. Additionally, 3DMA achieved ~98% absorbance (350–1500 nm). However, a lower surface temperature (39 °C) was observed on the surface while floating on the water. The unique resultant 3D architecture enhanced the extended

light path, multiple light scattering, and decreased light scattering at the liquid-to-material interface, which eventually improved the light absorption capacity. As a result, 3DMA achieved the evaporation rate of 1.41 kg/m$^2$h under 1 sun at solar steam efficiency of 88.7%. Additionally, the developed $Ti_3C_2T_x$ MXene-based porous structure was highly stable for 10 cycles at 30 min of each cycle. In this study, direct contact of 3DMA on water lost its light-to-heat towards the bulk water. Thus, expandable polyethylene foam (insulating layer) was wrapped around the architecture to minimize heat loss and improve the photothermal conversion efficiency.

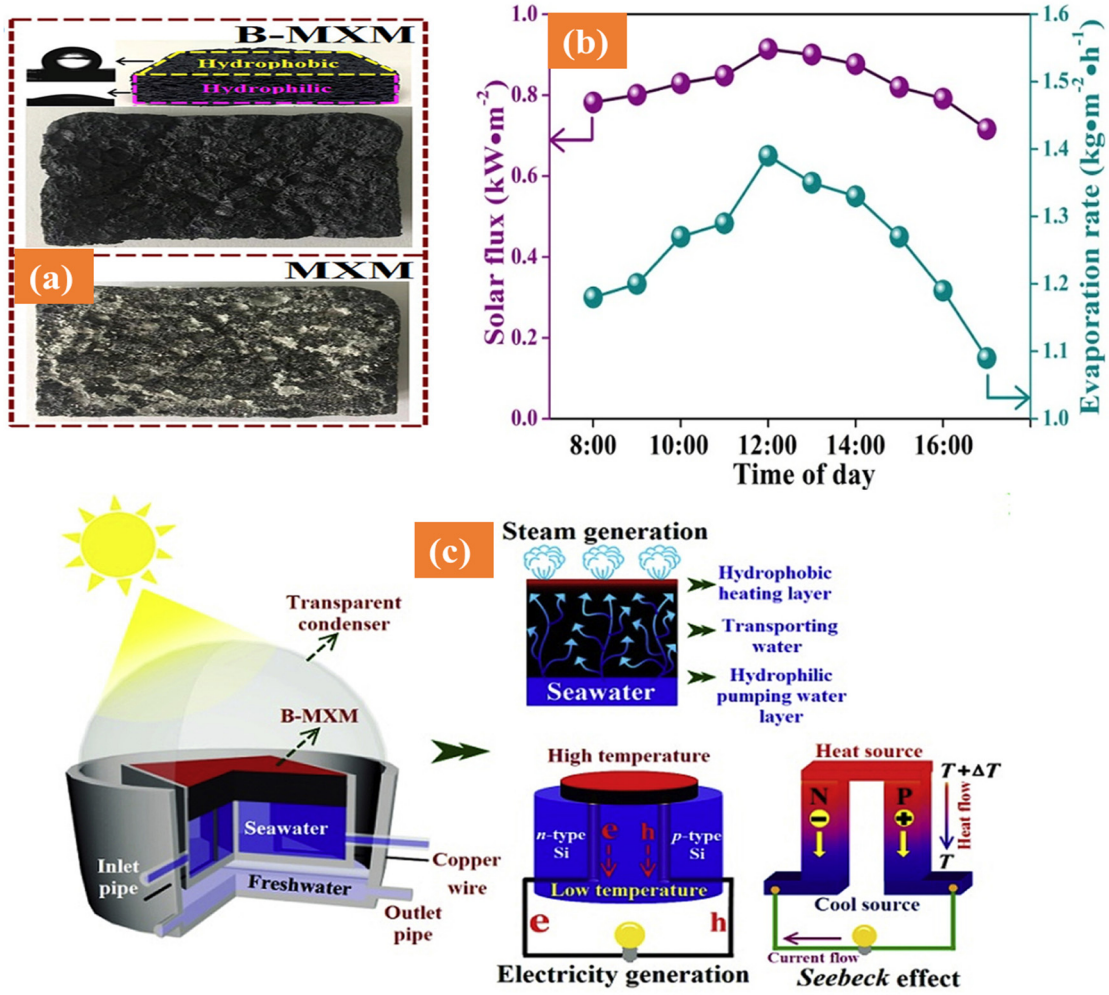


**Figure 6.** (**a**) Hydrophobic/hydrophilic bilayers of $Ti_3C_2$ MXene-based monolith with heat localization by hydrophobic nature, (**b**) corresponding evaporation rate at various time and solar intensities, and (**c**) implementation of simultaneous solar desalination and voltage measurements through temperature difference, using hydrophobic and hydrophilic $Ti_3C_2$ MXene layers (reprinted from Ref. [20], copyright with permission from Elsevier, 2020).

### *7.7. Nanocomposite*

In addition to the above pure 2D $Ti_3C_2$ MXene, the developing of 2D/2D hierarchical nanocomposites also raised its importance in solar steam generation. Very recently, Xu et al. [64] interrelated the $Ti_3C_2$ and $MoS_2$ for the development of an accordion-like-layer-structured 2D/2D $Ti_3C_2/MoS_2$ composite via the hydrothermal method. This composite provided broadband light absorption between 200 nm and 2500 nm. Figure 7a presents the surface morphology of the $Ti_3C_2/MoS_2$ composite at evenly distributed $MoS_2$ layers on accordion-like $Ti_3C_2$. Interestingly, both $Ti_3C_2$ and $MoS_2$ act as photothermal materials. Under this situation, a selective mass fraction of $Ti_3C_2$ (65 wt%) in the $Ti_3C_2/MoS_2$ composite (TM-3) achieved superior evaporation rate, compared to the other conditions

of $MoS_2$ (35, 50, and 80%). Additionally, an optical absorption capacity of 92.4% was achieved, which is higher than other counterparts as shown in Figure 7b. Moreover, TM-3 addressed lower transmission of light (3.77%) and reflection (3.78%). On the other hand, the achieved morphological features and large gaps between layers succeeded in multiple light reflections and refractions, which eventually boosted the improvement in the light absorption. Under the superior light absorption ability of TM-3, light-to-heat conversion was observed in the range of 28.5–55.3 °C within a short time of 4 min and reached 60.8 °C in 56 min. Under these constructive morphological features, TM-3 composite yielded the evaporation rate of 1.36 kg/m$^2$h, photothermal conversion efficiency of 87.2%, and strong light absorption capacity of 92.4% (Figure 7c).

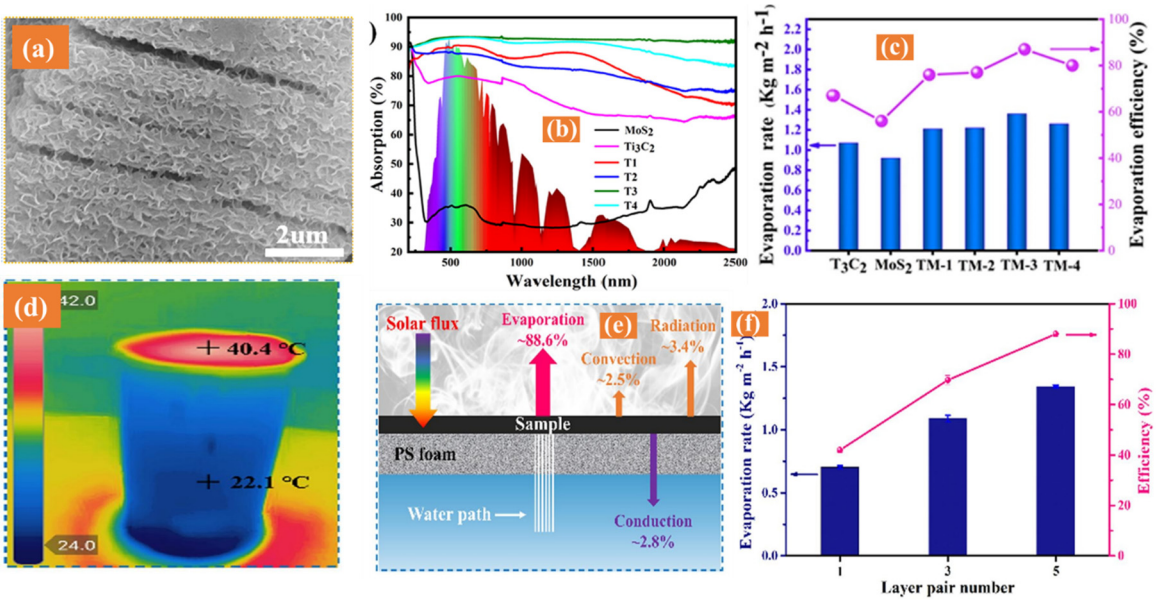


**Figure 7.** (**a**) Surface morphology of $Ti_3C_2/MoS_2$ composite at evenly distributed $MoS_2$ layers on accordion-like $Ti_3C_2$, (**b**) solar absorption behavior of pure $Ti_3C_2$, $MoS_2$, and various mass fractions of $MoS_2$ in $Ti_3C_2/MoS_2$, and (**c**) corresponding water evaporation rate and solar evaporation efficiency (reprinted from Ref. [64], copyright with permission from Elsevier, 2021), (**d**) variation in the temperature change on the surface and bottom of five times layer-by-layer grown $Ti_3C_2T_x$ MXene/CNT composite, (**e**) evaporation, convection, radiation, and thermal conduction rate during solar desalination, and (**f**) corresponding evaporation rate and light conversion efficiency of $Ti_3C_2T_x$ MXene/CNT at different layer growths (1, 3, and 5) (reprinted from Ref. [65], copyright with permission from Elsevier, 2021).

### *7.8. Other Morphologies*

In addition to the above constructive synthesis of various morphologies, HF-free (LiF/HCl) etched $Ti_3C_2$ (-OH,-F and -O) MXene nanosheets (pH of 5) were developed on carbon nanotube (CNT)–coated cotton fabric (MC) by the layer-by-layer assembly to highlight the solar evaporation under an intimate interfacial interaction [65]. Here, they found key electrostatic interaction and hydrogen bonding between $Ti_3C_2T_x$ MXene (negatively charged) and CNT (positively charged). The -OH, -F and -O functional groups raised on the $Ti_3C_2$ surface and -$NH_2$ developed on CNT, which provided the hydrophilic nature with cotton fabric (polar substrate). Additionally, hydrophilic MXenes were well dispersed in water. These features rapidly wetted the composite fabric for water transportation during the evaporation process. In such a way, selective layer-by-layer grown (five times) $Ti_3C_2T_x$ MXene/CNT composite $(MC)_5$ cotton fabric achieved the light absorption capacity of 93.5% (dry state) and 97.7% (wet state) throughout the solar spectrum (250–2500 nm). Specifically, the porous structure benefited from the light absorption and air–water interfacial area. Thus, the $(MC)_5$ cotton fabric achieved a surface temperature of 40.4°C under 1 sun in 10 min (Figure 7d). As a result, $(MC)_5$ achieved the evaporation rate of 1.35 kg/m$^2$h, which is 3.29 times higher than pure water (0.41 kg/m$^2$h) with an energy conversion evaporation

efficiency of 88.2 ± 0.9% (convection ~2.5%, radiation ~3.4% and conduction ~2.8%) as shown in Figure 7e,f. The lower thermal conducting behavior of $(MC)_5$ during the desalination process boosted the localization of heat on the surface, which eventually reduced the heat loss toward the surrounding environments. In other words, the thermal conductivity of pure water was 0.6 $Wm^{-1}K^{-1}$, which was higher than $(MC)_5$ at 0.12 $Wm^{-1}K^{-1}$. These results suggest the lower thermal conductivity of $Ti_3C_2T_x$ MXene-based composites, which boosted the water evaporation rate. Thus, $(MC)_5$ gained improvement in the evaporation rate compared to pure water. Overall, $Ti_3C_2T_x$ MXene/CNT cotton fabric composite achieved an efficient solar evaporation rate based on the following interesting factors: (i) low reflection, (ii) low thermal conductivity to reduce the convection heat to ambient (air), (iii) high optical absorption, and (iv) photothermal conversion. Table 2 presents the solar desalination activity of $Ti_3C_2$ MXene-based membrane, monolith, and porous morphologies.

**Table 2.** Summary of $Ti_3C_2$-based membrane, monolith, and porous morphologies for solar desalination.

| $Ti_3C_2$-Based Membrane, Monolith, and Porous Morphologies for Solar Desalination | | | | | | | |
|---|---|---|---|---|---|---|---|
| **$Ti_3C_2$-Based Composite (Optimized Condition)** | **$Ti_3C_2$ Functional Groups (Etching Process)** | **Solar Evaporation Efficiency (%) (1 Sun)** | **Surface Temperature (°C)** | **Stability** | **Solar Desalination Rate ($Kg/m^2h$)** | | **Ref** |
| | | | | | **Base Material** | **Resultant Composite** | |
| **Membrane** | | | | | | | |
| **$Ti_3C_2$** | HCl and LiF | 99.5 | 39 (10 min) | 200 h | 1.41 (hydrophilic) | 1.31 | [58] |
| **$Ti_3C_2T_x$** | HCl and LiF | — | 65.4 (5 min) | — | — | 1.33 | [59] |
| **$Cu_3BiS_3/Ti_3C_2$ (1:1)** | (O and OH) HCl and LiF | 87.11 | 62.3 | — | — | 1.32 | [60] |
| **$Ti_3C_2$** | HF | 84 | 75 | — | — | — | [39] |
| **PDA@ MXene** | HCl and LiF | 85.2 | 80 | — | PDA-1.157, $Ti_3C_2T_x$-1.095 | 1.276 | [61] |
| **Fluorinated porphyrin–$Ti_3C_2T_x$ MXene** | HCl and LiF | 86.4 | 66 | — | — | 1.41 | [57] |
| **$Ti_3C_2$/PVDF** | HF | — | 43.3 (10 min) | — | — | 0.98 | [62] |
| **Monolith** | | | | | | | |
| **$Ti_3C_2$ MXene** | — | 82.9 | 98 (upper surface), 30 (lower surface) | — | — | 1.39 | [20] |
| **Porous** | | | | | | | |
| **Carbonized melamine foam (CMF)@d-$Ti_3C_2$** | HCl and LiF | 84.6 | 38.5 (10 min) | — | $Ti_3C_2$-1.41 | 1.60 | [63] |
| **$Ti_3C_2T_x$** | HCl and LiF | 88.7 | 39 | — | — | 1.41 | [21] |
| **Nanocomposite** | | | | | | | |
| **$Ti_3C_2/MoS_2$** | — | 87.2 | 55.3 (4 min) | — | — | 1.36 | [64] |
| **Other morphologies** | | | | | | | |
| **MXene nanosheets on carbon nanotube coated cotton fabric** | -OH, -F and -O (HCl and LiF) | 88.2±0.9 | 40.4 | — | — | 1.35 | [65] |

## 8. Conclusions and Future Perspectives

The current review comprehensively summarized the potentiality of various morphological $Ti_3C_2$ MXene-based composites for the effective solar desalination of seawater for freshwater generation. It is concluded that the desalination process of $Ti_3C_2$ MXene greatly depends on the morphological features, which include aerogel, foam, hydrogel, membrane, monolith, and porous structures. The evolution of $Ti_3C_2$ MXene morphologies extended the water absorption capacity and light absorption toward the broadband region, thanks to

the exceptional photothermal conversion ability of the layer-structured 2D $Ti_3C_2$ MXenes. To date, the desalination of seawater using $Ti_3C_2$ MXene is still in its infancy. The $Ti_3C_2$ MXenes are significant for explaining the light-to-heat generation and heat localization on the surface for the successful evaporation of seawater into freshwater. Additionally, incident light was greatly absorbed inside the MXene through multiple light-reflection phenomena. Specifically, the intrinsic hydrophilic nature of the $Ti_3C_2$ MXene makes a potential path for water transportation channel toward the top of the surface. It was found that $Ti_3C_2$ MXenes prevailed with low radiation, low convection, and low thermal conduction, which eventually increased the light absorption and evaporation. The above-discussed concepts reveal that $Ti_3C_2$ MXenes are eco-friendly during the solar desalination of seawater. Due to scarce studies on the desalination ability of $Ti_3C_2$ MXenes, there are many constructive suggestions and perspectives:

1. The intrinsic hydrophilic nature and water absorption ability of layer-structured $Ti_3C_2$ MXenes determine its applicability in the field of eco-friendly solar desalination of seawater into freshwater.
2. In the contest of long-term stability, researchers should pay more attention toward membrane-based $Ti_3C_2$ MXenes for understanding efficient solar desalination. Thus, further research is necessary to understand the efficiency of $Ti_3C_2$ MXene membranes as a forerunner in solar desalination.
3. Due to the limited research on the $Ti_3C_2$ MXenes for solar desalination, it is further required to develop the wide band gap semiconductor material interaction with $Ti_3C_2$ MXenes for widening the solar light absorption. More research needs to be carried out in this direction.
4. The long-term stability of the layer-structured $Ti_3C_2$ MXenes is also a major challenge. However, surface modification through the selective termination groups shows great attention on the air–water interface for long-term stability.
5. Regarding the all-weather and complex conditions, there is infinite scope and opportunity for researchers to expand the potentiality of $Ti_3C_2$ MXenes for freshwater generation.
6. The developing of self-floating $Ti_3C_2$ MXenes with a hydrophilic nature has not been investigated. Thus, ceaseless efforts are required to accomplish the self-floating nature of $Ti_3C_2$ MXenes.
7. In addition to the self-floating nature, the salt-blocking nature during the desalination process significantly boosts the light absorption capacity and water transportation toward the top of the absorber. Such configurations are ideal for highly efficient solar desalination and long-term durability.
8. The oxidation stability of MXene during interaction with water under solar light illumination needs to be clearly explained.

In a word, this review provides new ideas for the design of novel 2D $Ti_3C_2$ MXenes-based composites for superior photothermal conversion and the solar desalination of seawater into freshwater.

**Author Contributions:** Conceptualization, A.S.; Writing-original draft preparation, A.S.; Writing-review and editing, J.-S.N.; supervision, J.-S.N.; funding acquisition, J.-S.N. All authors have read and agreed to the published version of the manuscript.

**Funding:** This work was funded by the National Research Foundation of Korea (NRF) by the Korea government (MSIT) (No. 2019R1A2C1008746).

**Acknowledgments:** This work was supported by the National Research Foundation of Korea (NRF) grant funded by the Korea government (MSIT) (No. 2019R1A2C1008746).

**Conflicts of Interest:** The authors declare no conflict of interest.

## References


1. Wang, Y.; Niu, B.; Zhang, X.; Lei, Y.; Zhong, P.; Ma, X. Review—$Ti_3C_2T_x$ MXene: An emerging two-dimensional layered material in water treatment. *ECS J. Solid State Sci. Technol.* **2021**, *10*, 47002. [CrossRef]
2. Hodges, B.C.; Cates, E.L.; Kim, J.-H. Challenges and prospects of advanced oxidation water treatment processes using catalytic nanomaterials. *Nat. Nanotechnol.* **2018**, *13*, 642–650. [CrossRef] [PubMed]
3. Elimelech, M.; Phillip, W.A. The future of seawater desalination: Energy, technology, and the environment. *Science* **2011**, *333*, 712–717. [CrossRef]
4. Prathapaneni, D.R.; Detroja, K. Optimal design of energy sources and reverse osmosis desalination plant with demand side management for cost-effective freshwater production. *Desalination* **2020**, *496*, 114741. [CrossRef]
5. Eljaddi, T.; Mendez, D.L.M.; Favre, E.; Roizard, D. Development of new pervaporation composite membranes for desalination: Theoretical and experimental investigations. *Desalination* **2021**, *507*, 115006. [CrossRef]
6. Liu, G.; Shen, J.; Liu, Q.; Liu, G.; Xiong, J.; Yang, J.; Jin, W. Ultrathin two-dimensional MXene membrane for pervaporation desalination. *J. Memb. Sci.* **2018**, *548*, 548–558. [CrossRef]
7. Davenport, D.M.; Deshmukh, A.; Werber, J.R.; Elimelech, M. High-pressure reverse osmosis for energy-efficient hypersaline brine desalination: Current status, design considerations, and research needs. *Environ. Sci. Technol. Lett.* **2018**, *5*, 467–475. [CrossRef]
8. Yu, F.; Wang, L.; Wang, Y.; Shen, X.; Cheng, Y.; Ma, J. Faradaic reactions in capacitive deionization for desalination and ion separation. *J. Mater. Chem. A* **2019**, *7*, 15999–16027. [CrossRef]
9. Lv, B.; Gao, C.; Xu, Y.; Fan, X.; Xiao, J.; Liu, Y.; Song, C. A self-floating, salt-resistant 3D Janus radish-based evaporator for highly efficient solar desalination. *Desalination* **2021**, *510*, 115093. [CrossRef]
10. Wang, Y.; Wu, Q.; Zhang, B.; Tian, L.; Li, K.; Zhang, X. Recent advances in transition metal carbide electrocatalysts for oxygen evolution reaction. *Catalysts* **2020**, *10*, 1164. [CrossRef]
11. Ta, Q.T.H.; Tran, N.M.; Noh, J.-S. Rice crust-like ZnO/$Ti_3C_2T_x$ MXene hybrid structures for improved photocatalytic activity. *Catalysts* **2020**, *10*, 1140. [CrossRef]
12. Hou, T.; Li, Q.; Zhang, Y.; Zhu, W.; Yu, K.; Wang, S.; Xu, Q.; Liang, S.; Wang, L. Near-infrared light-driven photofixation of nitrogen over $Ti_3C_2T_x/TiO_2$ hybrid structures with superior activity and stability. *Appl. Catal. B Environ.* **2020**, *273*, 119072. [CrossRef]
13. Shahzad, F.; Alhabeb, M.; Hatter, C.B.; Anasori, B.; Man Hong, S.; Koo, C.M.; Gogotsi, Y. Electromagnetic interference shielding with 2D transition metal carbides (MXenes). *Science* **2016**, *353*, 1137–1140. [CrossRef]
14. Jiang, X.; Kuklin, A.V.; Baev, A.; Ge, Y.; Ågren, H.; Zhang, H.; Prasad, P.N. Two-dimensional MXenes: From morphological to optical, electric, and magnetic properties and applications. *Phys. Rep.* **2020**, *848*, 1–58. [CrossRef]
15. Zhao, X.; Peng, L.M.; Tang, C.Y.; Pu, J.H.; Zha, X.J.; Ke, K.; Bao, R.Y.; Yang, M.B.; Yang, W. All-weather-available, continuous steam generation based on the synergistic photo-thermal and electro-thermal conversion by MXene-based aerogels. *Mater. Horizons* **2020**, *7*, 855–865. [CrossRef]
16. Xie, X.; Chen, C.; Zhang, N.; Tang, Z.-R.; Jiang, J.; Xu, Y.-J. Microstructure and surface control of MXene films for water purification. *Nat. Sustain.* **2019**, *2*, 856–862. [CrossRef]
17. Fan, X.; Yang, Y.; Shi, X.; Liu, Y.; Li, H.; Liang, J.; Chen, Y. A MXene-based hierarchical design enabling highly efficient and stable solar-water desalination with good salt resistance. *Adv. Funct. Mater.* **2020**, *30*, 2007110. [CrossRef]
18. Fan, D.; Lu, Y.; Zhang, H.; Xu, H.; Lu, C.; Tang, Y.; Yang, X. Synergy of photocatalysis and photothermal effect in integrated 0D perovskite oxide/2D MXene heterostructures for simultaneous water purification and solar steam generation. *Appl. Catal. B Environ.* **2021**, *295*, 120285. [CrossRef]
19. Ding, M.; Xu, H.; Chen, W.; Yang, G.; Kong, Q.; Ng, D.; Lin, T.; Xie, Z. 2D laminar maleic acid-crosslinked MXene membrane with tunable nanochannels for efficient and stable pervaporation desalination. *J. Memb. Sci.* **2020**, *600*, 117871. [CrossRef]
20. Zhang, Q.; Chen, S.; Fu, Z.; Yu, H.; Quan, X. Temperature-difference-induced electricity during solar desalination with bilayer MXene-based monoliths. *Nano Energy* **2020**, *76*, 105060. [CrossRef]
21. Zhao, X.; Zha, X.-J.; Pu, J.-H.; Bai, L.; Bao, R.-Y.; Liu, Z.-Y.; Yang, M.-B.; Yang, W. Macroporous three-dimensional MXene architectures for highly efficient solar steam generation. *J. Mater. Chem. A* **2019**, *7*, 10446–10455. [CrossRef]
22. Su, T.; Hood, Z.D.; Naguib, M.; Bai, L.; Luo, S.; Rouleau, C.M.; Ivanov, I.N.; Ji, H.; Qin, Z.; Wu, Z. Monolayer $Ti_3C_2T_x$ as an effective co-catalyst for enhanced photocatalytic hydrogen production over $TiO_2$. *ACS Appl. Energy Mater.* **2019**, *2*, 4640–4651. [CrossRef]
23. Cheng, X.; Zu, L.; Jiang, Y.; Shi, D.; Cai, X.; Ni, Y.; Lin, S.; Qin, Y. A titanium-based photo-Fenton bifunctional catalyst of mp-MXene/$TiO_{2-x}$ nanodots for dramatic enhancement of catalytic efficiency in advanced oxidation processes. *Chem. Commun.* **2018**, *54*, 11622–11625. [CrossRef]
24. Shahzad, A.; Rasool, K.; Nawaz, M.; Miran, W.; Jang, J.; Moztahida, M.; Mahmoud, K.A.; Lee, D.S. Heterostructural $TiO_2/Ti_3C_2T_x$ (MXene) for photocatalytic degradation of antiepileptic drug carbamazepine. *Chem. Eng. J.* **2018**, *349*, 748–755. [CrossRef]
25. Low, J.; Zhang, L.; Tong, T.; Shen, B.; Yu, J. $TiO_2$/MXene $Ti_3C_2$ composite with excellent photocatalytic $CO_2$ reduction activity. *J. Catal.* **2018**, *361*, 255–266. [CrossRef]
26. Chen, Y.-H.; Qi, M.-Y.; Li, Y.-H.; Tang, Z.-R.; Wang, T.; Gong, J.; Xu, Y.-J. Activating two-dimensional $Ti_3C_2T_x$-MXene with single-atom cobalt for efficient $CO_2$ photoreduction. *Cell Rep. Phys. Sci.* **2021**, *2*, 100371. [CrossRef]

27. Li, M.; Liu, X.; Wang, L.; Hou, F.; Dou, S.X.; Liang, J. Rational design on photo(electro)catalysts for artificial nitrogen looping. *EcoMat* **2021**, *3*, e12096. [CrossRef]
28. Zhu, J.; Zhu, M.; Shi, Q.; Wen, F.; Liu, L.; Dong, B.; Haroun, A.; Yang, Y.; Vachon, P.; Guo, X.; et al. Progress in TENG technology—A journey from energy harvesting to nanoenergy and nanosystem. *EcoMat* **2020**, *2*, e12058. [CrossRef]
29. Zhang, M.; Héraly, F.; Yi, M.; Yuan, J. Multitasking tartaric-acid-enabled, highly conductive, and stable MXene/conducting polymer composite for ultrafast supercapacitor. *Cell Rep. Phys. Sci.* **2021**, *2*, 100449. [CrossRef]
30. Saranin, D.; Pescetelli, S.; Pazniak, A.; Rossi, D.; Liedl, A.; Yakusheva, A.; Luchnikov, L.; Podgorny, D.; Gostischev, P.; Didenko, S.; et al. Transition metal carbides (MXenes) for efficient NiO-based inverted perovskite solar cells. *Nano Energy* **2021**, *82*, 105771. [CrossRef]
31. Bati, A.S.R.; Sutanto, A.A.; Hao, M.; Batmunkh, M.; Yamauchi, Y.; Wang, L.; Wang, Y.; Nazeeruddin, M.K.; Shapter, J.G. Cesium-doped $Ti_3C_2T_x$ MXene for efficient and thermally stable perovskite solar cells. *Cell Rep. Phys. Sci.* **2021**, *2*, 100598. [CrossRef]
32. Ihsanullah, I. Potential of MXenes in water desalination: Current status and perspectives. *Nano-Micro Lett.* **2020**, *12*, 72. [CrossRef] [PubMed]
33. Li, L.; Wang, C.; Feng, K.; Huang, D.; Wang, K.; Li, Y.; Jiang, F. Kesterite $Cu_2ZnSnS_4$ thin-film solar water-splitting photovoltaics for solar seawater desalination. *Cell Rep. Phys. Sci.* **2021**, *2*, 100468. [CrossRef]
34. Morciano, M.; Fasano, M.; Boriskina, S.V.; Chiavazzo, E.; Asinari, P. Solar passive distiller with high productivity and marangoni effect-driven salt rejection. *Energy Environ. Sci.* **2020**, *13*, 3646–3655. [CrossRef]
35. Zhu, Z.; Xu, Y.; Luo, Y.; Wang, W.; Chen, X. Porous evaporators with special wettability for low-grade heat-driven water desalination. *J. Mater. Chem. A* **2021**, *9*, 702–726. [CrossRef]
36. Chaudhuri, K.; Alhabeb, M.; Wang, Z.; Shalaev, V.M.; Gogotsi, Y.; Boltasseva, A. Highly broadband absorber using plasmonic titanium carbide (MXene). *ACS Photonics* **2018**, *5*, 1115–1122. [CrossRef]
37. Zhang, Y.; Xiong, T.; Nandakumar, D.K.; Tan, S.C. Structure architecting for salt-rejecting solar interfacial desalination to achieve high-performance evaporation with in situ energy generation. *Adv. Sci.* **2020**, *7*, 1903478. [CrossRef]
38. Ghidiu, M.; Lukatskaya, M.R.; Zhao, M.-Q.; Gogotsi, Y.; Barsoum, M.W. Conductive two-dimensional titanium carbide 'clay' with high volumetric capacitance. *Nature* **2014**, *516*, 78–81. [CrossRef]
39. Li, R.; Zhang, L.; Shi, L.; Wang, P. MXene $Ti_3C_2$: An effective 2D light-to-heat conversion material. *ACS Nano* **2017**, *11*, 3752–3759. [CrossRef]
40. Liu, H.; Huang, Z.; Liu, K.; Hu, X.; Zhou, J. Interfacial solar-to-heat conversion for desalination. *Adv. Energy Mater.* **2019**, *9*, 1900310. [CrossRef]
41. Liu, G.; Chen, T.; Xu, J.; Yao, G.; Xie, J.; Cheng, Y.; Miao, Z.; Wang, K. Salt-Rejecting solar interfacial evaporation. *Cell Rep. Phys. Sci.* **2021**, *2*, 100310. [CrossRef]
42. Han, X.; Zang, L.; Zhang, S.; Dou, T.; Li, L.; Yang, J.; Sun, L.; Zhang, Y.; Wang, C. Hydrophilic polymer-stabilized porous composite membrane for water evaporation and solar desalination. *RSC Adv.* **2020**, *10*, 2507–2512. [CrossRef]
43. Yao, J.; Yang, G. An efficient solar-enabled 2D layered alloy material evaporator for seawater desalination. *J. Mater. Chem. A* **2018**, *6*, 3869–3876. [CrossRef]
44. Thoai, D.N.; Hoai Ta, Q.T.; Truong, T.T.; Van Nam, H.; Van Vo, G. Review on the recent development and applications of three dimensional (3D) photothermal materials for solar evaporators. *J. Clean. Prod.* **2021**, *293*, 126122. [CrossRef]
45. Fengler, C.; Arens, L.; Horn, H.; Wilhelm, M. Desalination of seawater using cationic poly(acrylamide) hydrogels and mechanical forces for separation. *Macromol. Mater. Eng.* **2020**, *305*, 2000383. [CrossRef]
46. Ying, L.; Zhu, H.; Li, H.; Zhu, Z.; Sun, S.; Wang, X.; Lu, S.; Du, M. Heterostructure design of $Cu_2O/Cu_2S$ core/shell nanowires for solar-driven photothermal water vaporization towards desalination. *Sustain. Energy Fuels* **2020**, *4*, 6023–6029. [CrossRef]
47. Yang, Y.; Zhao, R.; Zhang, T.; Zhao, K.; Xiao, P.; Ma, Y.; Ajayan, P.M.; Shi, G.; Chen, Y. Graphene-based standalone solar energy converter for water desalination and purification. *ACS Nano* **2018**, *12*, 829–835. [CrossRef]
48. Kospa, D.A.; Ahmed, A.I.; Samra, S.E.; Ibrahim, A.A. High efficiency solar desalination and dye retention of plasmonic/reduced graphene oxide based copper oxide nanocomposites. *RSC Adv.* **2021**, *11*, 15184–15194. [CrossRef]
49. Naguib, M.; Kurtoglu, M.; Presser, V.; Lu, J.; Niu, J.; Heon, M.; Hultman, L.; Gogotsi, Y.; Barsoum, M.W. Two-dimensional nanocrystals: Two-dimensional nanocrystals produced by exfoliation of $Ti_3AlC_2$ (Adv. Mater. 37/2011). *Adv. Mater.* **2011**, *23*, 4207. [CrossRef]
50. Xie, Z.; Peng, Y.-P.; Yu, L.; Xing, C.; Qiu, M.; Hu, J.; Zhang, H. Solar-inspired water purification based on emerging 2D materials: Status and challenges. *Sol. RRL* **2020**, *4*, 1900400. [CrossRef]
51. Sreedhar, A.; Noh, J.-S. Interfacial engineering insights of promising monolayer 2D $Ti_3C_2$ MXene anchored flake-like ZnO thin films for improved PEC water splitting. *J. Electroanal. Chem.* **2021**, *883*, 115044. [CrossRef]
52. Biener, J.; Stadermann, M.; Suss, M.; Worsley, M.A.; Biener, M.M.; Rose, K.A.; Baumann, T.F. Advanced carbon aerogels for energy applications. *Energy Environ. Sci.* **2011**, *4*, 656. [CrossRef]
53. Ming, X.; Guo, A.; Zhang, Q.; Guo, Z.; Yu, F.; Hou, B.; Wang, Y.; Homewood, K.P.; Wang, X. 3D macroscopic graphene oxide/MXene architectures for multifunctional water purification. *Carbon N.Y.* **2020**, *167*, 285–295. [CrossRef]
54. Zhang, Q.; Yi, G.; Fu, Z.; Yu, H.; Chen, S.; Quan, X. Vertically aligned janus MXene-based aerogels for solar desalination with high efficiency and salt resistance. *ACS Nano* **2019**, *13*, 13196–13207. [CrossRef]

55. Lin, H.; Wang, X.; Yu, L.; Chen, Y.; Shi, J. Two-dimensional ultrathin MXene ceramic nanosheets for photothermal conversion. *Nano Lett.* **2017**, *17*, 384–391. [CrossRef] [PubMed]
56. Guo, Y.; Yu, G. Engineering hydrogels for efficient solar desalination and water purification. *Accounts Mater. Res.* **2021**, *2*, 374–384. [CrossRef]
57. Zhang, B.; Gu, Q.; Wang, C.; Gao, Q.; Guo, J.; Wong, P.W.; Liu, C.T.; An, A.K. Self-assembled hydrophobic/hydrophilic porphyrin-$Ti_3C_2T_x$ MXene janus membrane for dual-functional enabled photothermal desalination. *ACS Appl. Mater. Interfaces* **2021**, *13*, 3762–3770. [CrossRef] [PubMed]
58. Zhao, J.; Yang, Y.; Yang, C.; Tian, Y.; Han, Y.; Liu, J.; Yin, X.; Que, W. A hydrophobic surface enabled salt-blocking 2D $Ti_3C_2$ MXene membrane for efficient and stable solar desalination. *J. Mater. Chem. A* **2018**, *6*, 16196–16204. [CrossRef]
59. Li, K.; Chang, T.; Li, Z.; Yang, H.; Fu, F.; Li, T.; Ho, J.S.; Chen, P. Biomimetic MXene textures with enhanced light-to-heat conversion for solar steam generation and wearable thermal management. *Adv. Energy Mater.* **2019**, *9*, 1901687. [CrossRef]
60. Wang, Z.; Yu, K.; Gong, S.; Mao, H.; Huang, R.; Zhu, Z. $Cu_3BiS_3$/MXenes with excellent solar–thermal conversion for continuous and efficient seawater desalination. *ACS Appl. Mater. Interfaces* **2021**, *13*, 16246–16258. [CrossRef]
61. Zhao, X.; Zha, X.-J.; Tang, L.-S.; Pu, J.-H.; Ke, K.; Bao, R.-Y.; Liu, Z.; Yang, M.-B.; Yang, W. Self-assembled core-shell polydopamine@MXene with synergistic solar absorption capability for highly efficient solar-to-vapor generation. *Nano Res.* **2020**, *13*, 255–264. [CrossRef]
62. Peng, H.; Zhu, K.; Li, C.; Xiao, Y.; Ye, M. $Ti_3C_2$/PVDF membrane for efficient seawater desalination based on interfacial solar heating. *Water Supply* **2021**, *21*, 918–926. [CrossRef]
63. Ju, M.; Yang, Y.; Zhao, J.; Yin, X.; Wu, Y.; Que, W. Macroporous 3D MXene architecture for solar-driven interfacial water evaporation. *J. Adv. Dielectr.* **2019**, *9*, 1950047. [CrossRef]
64. Xu, R.; Wei, N.; Li, Z.; Song, X.; Li, Q.; Sun, K.; Yang, E.; Gong, L.; Sui, Y.; Tian, J.; et al. Construction of hierarchical 2D/2D $Ti_3C_2/MoS_2$ nanocomposites for high-efficiency solar steam generation. *J. Colloid Interface Sci.* **2021**, *584*, 125–133. [CrossRef]
65. Wang, Y.; Qi, Q.; Fan, J.; Wang, W.; Yu, D. Simple and robust MXene/carbon nanotubes/cotton fabrics for textile wastewater purification via solar-driven interfacial water evaporation. *Sep. Purif. Technol.* **2021**, *254*, 117615. [CrossRef]